Construction of DNA-Nanoparticle Conjugates for Applications in Molecular Electronics and Biosensing

Master Thesis by

Kasper Risgaard Jensen

Project period: *September 1st 2008 to July 31st 2009*

Institute of Physics and Nanotechnology, Aalborg University, Aalborg

AALBORG UNIVERSITET

Institut for Fysik og Nanoteknologi
Skjernvej 4C
9220 Aalborg Ø.
Tlf. 96659215
Fax 98156502

Title: Construction of DNA-Nanoparticle Conjugates for Applications in Molecular Electronics and Biosensing

Project Period: September 1st 2008 to July 31st 2009

Master Thesis

Author:
Kasper Risgaard Jensen _____

Supervisor:
Leonid Gurevich

Circulation: 5
Number of pages: 60

Abstract

This study is focused on the production of DNA-silver nanoparticle conjugates for applications in e.g. plasmonic biosensors and molecular electronics. Most research in DNA-nanoparticle conjugates is focused on the use of gold nanoparticles as these are more stable than silver nanoparticles. However, silver has a higher extinction coefficient and a sharper localized surface plasmon resonance than gold, which may provide higher sensitivity in plasmonic sensors. Additionally, the conductivity of silver is higher than that of gold, and this makes it interesting from a molecular electronics point of view.

Here we report a method for the construction of DNA-silver nanoparticle conjugates in only 2 hours. The binding of DNA to Ag nanoparticles is based on the specific interaction between phosphorothioate groups on the DNA and silver. In this respect, phosphorothioated single stranded DNA and hairpin structured DNA modified with phosphorothioate groups in the loop region is used. Single stranded random sequence DNA is used as a reference in order to be able to distinguish phosphorothioate binding from non-specific binding. Furthermore, the binding of phosphorothioated ATP, with ATP used as a reference, is examined in order to determine its stabilizing effect.

Absorbance measurements and gel electrophoresis experiments showed that phosphorothioated single stranded DNA provided the largest stabilizing effect for the silver nanoparticles. Hairpin structured DNA with a phosphorothioated loop region provided the second highest stabilization, and single stranded DNA without phosphorothioate groups provided the smallest stabilizing effect. Hereby the specific interaction between phosphorothioate groups and silver nanoparticles was confirmed. In contrary to what was observed with DNA, the presence of a phosphorothioate group on ATP did not improve the stabilizing ability of the molecule, since aggregation was induced instead.

As a second part of this study we compare the sensitivity of surface plasmon polariton based surface plasmon resonance biosensors. The sensors involve the DNA binding peptide indolicidin-4 and either double stranded DNA linked to a gold film or double stranded DNA-silver nanoparticle conjugates linked to a gold film. The presence of the nanoparticles is envisaged to enhance the sensor sensitivity. It is expected that the binding of indolicidin-4 to the DNA will result in a change of the DNA conformation, and that this will change the nanoparticle-film distance when the indolicidin-4 is bound to the conjugates. The distance change is expected to be visible as scattering of the gold film surface plasmon polariton by the nanoparticle is distance dependent. The linking of double stranded DNA and the conjugates to the gold film was confirmed by surface plasmon resonance spectroscopy, and furthermore the linking of the conjugates was confirmed by atomic force microscopy. With the two sensors a larger shift of the resonance angle was observed at indolicidin-4 binding to double stranded DNA compared to binding to double stranded DNA-silver nanoparticle conjugates. Furthermore, the expected change in surface plasmon polariton scattering at binding to the conjugates was not clearly observed. However, association and dissociation rate constants of $432 M^{-1}s^{-1}$ and $0.00002 s^{-1}$ for the binding of indolicidin-4 to double stranded DNA were obtained, and to our knowledge this is the first time kinetic constants for this interaction has been reported.

Preface

This master thesis is authored by Kasper Risgaard Jensen at Institute of Physics and Nanotechnology, Aalborg University. The thesis was made in the period from September 1st 2008 to July 31st 2009. The title of the thesis is "Construction of DNA-Nanoparticle Conjugates for Applications in Molecular Electronics and Biosensing".

The report is divided into 7 chapters and 1 appendix. The figures, tables, and equations are continuously enumerated after which chapter they are placed in. For instance, figure or table 2 in chapter 5 is given the number 5.2.

In-text references are as follows: ["Number"]. The cited references are numbered in order of appearance and they may be found in the bibliography on the basis of the numbers. In the bibliography, the references of articles are presented as follows: Authors (year). "*Title*". Journal volume (issue): pages. References to books are presented in the following manner: Authors (year). "*Title*". City, Publisher, Edition, whereas references to book sections are presented as: Authors (year). "*Title*". Book Title. Editor. City, Publisher, Edition: Pages. References to a thesis is presented as: Authors (year). "Title". Academic department, University, City. **Degree**. A reference to conference proceedings is presented as: Authors (year of conference). Title. Conference name, conference location, Publisher. References to online sources will in the bibliography be presented as follows: Name, URL address, date accessed.

Acknowledgements

I would like to thank the following for contributing to this project:

- Associate professor P. Fojan for supplying IL-4 and for helpful advice.
- Professor A. Kotlyar for helpful advice.
- The Novo Scholarship Programme for financial support.

Abbreviations

Ag	silver
ATP	adenosine 5'-triphosphate
ATR	attenuated total reflection
Au	gold
dsDNA	double stranded DNA
ΔG	Gibbs free energy increment
IL	indolicidin
IL-4	IL with tryptophan 4 retained and remaining substituted by leucines
k_a	association rate constant
k_d	dissociation rate constant
K_D	equilibrium binding constant
LSP	localized surface plasmon
pto-ATP	adenosine 5′-[γ-thio]triphosphate
Rmax	maximum response
SPP	surface plasmon polariton
SPR	surface plasmon resonance
ssDNA	single stranded DNA
TE	transverse electric
TM	transverse magnetic
Tm	melting temperature

Contents

1 Introduction

The field of plasmonics contains two main ingredients, namely surface plasmon polaritons (SPPs) present at metallic interfaces and localized surface plasmons (LSPs) present in metallic nanostructures. It aims to describe the interaction between electromagnetic radiation and conduction electrons at the metallic interfaces or in the metallic nanostructures. Both SPPs and LSPs were described for the first time around the beginning of the 20th century[1]. Though, the practical use of the plasmonics phenomenon, in the form of sensors based on surface plasmon resonance (SPR) at a metal surface, was not introduced until the early 1980s[2]. However, today many optical biosensors rely on surface plasmon resonance[3].

SPR sensors may be divided into two types[3]. One type of sensors is based on the fact that the resonance conditions required to excite the plasmons depend on the refractive index of the dielectric medium next to the metallic interface or around the metallic nanoparticle. Local refractive index changes may for instance be caused by biomolecular interactions at the metal-dielectric interface. This technique is widely used for sensors based on SPR changes in thin metal films, and spectrometers based on this technique are commercially available[4,5]. The technique may however also be used for detection of binding of biomolecules at the surface of metallic nanoparticles[3]. In the second type of SPR sensors it is utilized that plasmons couple at short distances and thereby shifts the SPR conditions. This may e.g. be used in sensors for determination of DNA hybridization by linking each of the hybridizing strands to a noble metal nanoparticle[6]. The hybridization then brings the particles into close proximity whereby the SPR resonance condition shifts. Linking of DNA to a noble metal particle was demonstrated for the first time in 1996 by Mirkin *et al.* and Alivisatos *et al*. who linked DNA to gold (Au) nanoparticles[7,8]. Au nanoparticles are commonly preferred due to a relatively high chemical stability of this metal compared to e.g. silver (Ag)[3]. However, Ag nanoparticles exhibits sharper resonances, a higher extinction coefficient and the highest conductivity and reflectivity among all metals, and the shift caused by coupling of plasmons in nanoparticles is higher for an Ag system than for an Au system[9,10,11,12]. A common method for production of DNA-Au nanoparticle conjugates is by introducing a thiol-linker at one end of the DNA molecule, whereby an Au-thiol bond may be formed. Though, this method does not produce stable DNA-Ag nanoparticle conjugates[6,13]. However, if a method for the production of sufficiently stable Ag nanoparticles along with a method for linking of DNA could be developed, Ag nanoparticles are more applicable than Au particles in some cases due to the higher sensitivity attained with Ag.

Detection of small molecules interacting with double stranded DNA (dsDNA) linked to a thin metal film has been performed with SPR sensors monitoring the refractive index change[14]. Still, the smaller the interacting molecule the lower does the SPR response become. Therefore, a method for enhancing the signal is required. In this respect, coupling of an Ag nanoparticle conjugated to the dsDNA would enable coupling of the LSP in the nanoparticle and the SPP in the metal film, or when off the LSP resonance, scattering of the SPP by the nanoparticle is enabled. The coupling has been reported to be very sensitive to the distance between the nanoparticle and the metal film[15], and a pH sensor based on the phenomenon has already been produced by Tokareva *et al.* (2004)[16]. It is hypothesized that

this enables detection of the binding of molecules which alter the DNA conformation at binding to dsDNA interlinking a nanoparticle and a metal film. The detection is facilitated by the change in the nanoparticle-film distance caused by the conformational change.

Additionally, the setup with a DNA-Ag nanoparticle conjugate linked to a metal film may be used for measuring the electron transport through the DNA. This is encouraged by the fact that DNA is speculated to be applicable for the design of molecular electronics due to the possibility to 'program' the DNA assembly. However, there have been controversies about the conduction mechanism and the conductive qualities of DNA[17]. In this respect the proposed setup may facilitate measurements on the electron transport in the DNA in order to eventually overcome these controversies.

1.1 Aim of Study

In this study the aim is to develop a method for stabilization of Ag nanoparticles and a method to produce DNA-Ag nanoparticle conjugates. As a further step the aim is to link the conjugates to an Au film in order to construct a biosensor based on the scattering of SPPs in the metal film by the nanoparticles.

The strategy used, is to examine the ability of mononucleotides and short DNA strands modified with phosphorothioate groups to stabilize Ag nanoparticles. It is hypothesized that the phosphorothioate groups provide specific binding sites. In this respect, the stabilizing effect of adenosine 5'-[γ-thio]triphosphate (pto-ATP) on Ag nanoparticles is investigated with the use of adenosine 5'-triphosphate (ATP) as a reference. Furthermore the stabilizing effect of hairpin structured DNA modified with phosphorothioate groups in the loop region and single stranded DNA modified with phosphorothioate groups at the 5' end is examined with random sequence single stranded DNA used as a reference. The production of DNA-Ag nanoparticle conjugates is also attempted with single stranded phosphorothioated DNA and hairpin DNA with a phosphorothioated loop region. The 5' end of the hairpin DNA is modified with a disulphide linker in order to facilitate linking of the conjugate to an Au film. Linking of the conjugate with single stranded DNA is facilitated by linking of a complementary DNA strand to the Au film which is followed by the hybridization of the two DNA strands. Binding of an analogue of the antimicrobial peptide indolicidin (IL) to the dsDNA-Ag nanoparticle conjugates linked to the Au film is investigated in order to test the biosensor concept.

In the remainder of this chapter theory about nanoparticle stabilization, SPR, and IL is presented to provide an overview of the concepts that needs to be taken into account to achieve the aim of this study.

1.2 Stabilization of Nanoparticles

A suspension of lyophobic colloids, such as metal nanoparticles, is thermodynamically unstable[18]. That is, the free energy of the state with nanoparticles in suspension is higher than the free energy of the state in which the particles are aggregated. However, aggregation may be prevented if a sufficiently high particle interaction energy barrier is present[18,19]. The presence of stabilizing agents on the surface of the nanoparticles can provide the required energy barrier whereby the nanoparticles are kept in a metastable state. In this respect electrostatic stabilization, steric stabilization, or a combination of the two, called electrosteric stabilization, is possible[19,20,21].

1.2.1 DLVO Theory

A theory for the stability of lyophobic colloidal suspensions was published independently by Derjaguin and Landau (1941) and Verwey and Overbeek (1948), and the theory is now known as the DLVO theory[22]. According to this theory the overall interaction potential (W_t) between two surfaces can be described as the sum of the attractive (W_a) and repulsive (W_r) potentials, as depicted in Equation 1.1[18].

$$W_t = W_a + W_r \qquad \textbf{Equation 1.1}$$

The attractive contribution to the overall interaction potential originates from the van der Waals force, whereas the repulsive contribution is caused by interpenetration of similarly charged diffuse double layers at the surfaces[18,23]. This is also known as electric double layer repulsion.

The van der Waals Force

The van der Waals force between two polar molecules is made up of three contributions, namely the orientation force, the induction force, and the dispersion force. These three contributions all behave as r^{-6} where r is the distance between the centres of the molecules. Hence, the van der Waals interaction potential between two polar molecules may be written as follows[22].

$$w_{vdw}(r) = -\frac{C_{vdw}}{r^6} = -\frac{C_{orient} + C_{ind} + C_{disp}}{r^6} \qquad \textbf{Equation 1.2}$$

The orientation force occurs between permanent dipoles and it is coulombic in nature. In accordance with Coulomb's law the interaction energy between two charges Q_1 and Q_2 can be written as $w(r) = \frac{Q_1 Q_2}{4\pi\varepsilon_0 \varepsilon r}$, where ε is the relative electric permittivity of the medium in which the interaction takes place and r is the distance between the charges[22,24]. This interaction energy can be used for calculation of the dipolar interaction energy by considering dipoles as consisting of two point charges, $+q$ and $-q$, separated by a distance l. The dipolar interaction energy behaves as r^{-3} where r is the distance between the centres of the dipoles. However, in liquid solutions the coulombic interaction is reduced due to a higher permittivity of the liquid compared to vacuum, and the thermal energy always exceeds the dipolar interaction energy. Therefore molecules are not bound due to dipolar interactions. Hence, the dipoles are relatively free to rotate, but as the Boltzmann weighting factor puts more weight to the orientations with lower energy the interaction potential between two permanent dipoles is not zero when angle-averaged. The angle-averaged interaction potential behaves as r^{-6} instead of as r^{-3} when not angle-averaged[22].

The induction force occurs between a permanent and an induced dipole. Like the orientation force this is also smaller than the thermal energy and it behaves as r^{-6} when angle-averaged[22].

The final of the three forces is the dispersion force, which acts between all atoms and molecules, and is therefore always present. It is quantum mechanical in origin, though it may be understood by considering a neutral molecule that has no dipole moment when time-averaged. However, the molecule instantaneously acquires a dipole moment due to a separation between the electrons and the protons. This instantaneous dipole is then able to

induce a dipole in a neighbouring molecule, whereby an attractive force arises between the molecules. The attractive force is non-zero when time-averaged and behaves as r^{-6} [22].

When considering interactions between particles instead of molecules the van der Waals potential can be found by summing the potentials between the molecules making up the particles[22]. The van der Waals potential between two spherical particles has been calculated by Hamaker[25] and may be calculated from the equation below, in which R is the distance between the centres of the particles, and r_1 and r_2 are the particle radii[23].

$$W_{vdw} = -\frac{A}{6}\left\{\frac{2r_1r_2}{R^2-(r_1+r_2)^2}+\frac{2r_1r_2}{R^2-(r_1-r_2)^2}+ln\frac{R^2-(r_1+r_2)^2}{R^2-(r_1-r_2)^2}\right\} \qquad \textbf{Equation 1.3}$$

In this equation A is the Hamaker constant. This constant was introduced by Hamaker[25] as $A = \pi^2 C_{vdw}\rho_1\rho_2$, where ρ_1 and ρ_2 are the number of atoms per unit volume in the two particles. The van der Waals potential between two particles composed of the same material is always negative, which means that the interparticle force is attractive[22,25]. The derivation of the van der Waals potential between particles based on the additivity approach however ignores the influence of neighbouring molecules on the interaction between any pair of molecules. Hence, the effect of the medium wherein the interacting particles are immersed is also ignored. This omission may be circumvented by using a continuum theory in which the atomic structure is ignored for calculation of the Hamaker constant, whereas the remainder of Equation 1.3 still applies[22]. According to Kim *et al.* (2005) the Hamaker constant of gold particles is in the range of $1\text{-}4\cdot10^{-19}$J [23].

The Electric Double Layer

According to the DLVO theory the attractive van der Waals force is counteracted by a repulsive force originating from surface charges on the interacting particles. Though, in electrolyte solution the surface charge is balanced by an equal but opposite charge from counterions, which builds up in the region next to the surface. Part of the counterions is bound more or less tightly in a layer at the surface called the Stern layer, whereas the others form a second layer called the diffuse electric double layer. The counterions in this layer are subject to rapid thermal motion, and the ion concentration decays exponentially away from the surface[22]. Charging of a surface may e.g. be caused by adsorption of ions or binding of charged molecules such as DNA. An example of charging by adsorption of ions is the chemical synthesis of gold and silver nanoparticles by reduction of auric acid or silver nitrateby citrate or borohydride, respectively. The nanoparticles formed when the gold and silver ions are reduced acquire a surface charge due to adsorption of citrate or borate ions, whereby they are stabilized[26,27].

Overall a surface with its associated electric double layer is neutral. However, when two surfaces approach each other and the electric double layers start to overlap repulsion between the surfaces occurs. At constant surface potentials below ~25mV the interaction potential between two spherical particles of radius r and separation R between the particle surfaces can be approximated by[22]:

$$W_{elect} = 2\pi r\varepsilon\varepsilon_0\psi_0^2 e^{-\kappa R} \qquad \textbf{Equation 1.4}$$

where ε is the relative electric permittivity of the solvent, ε_0 is the vacuum permittivity, ψ_0 is the surface potential of the particles, and κ is the inverse of the Debye length. The Debye

length is a measure of the diffuse electric double layer thickness, and it depends solely on the solvent properties such as ionic strength[22]. In Figure 1.1 the DLVO interaction potential between two particles is depicted, which is the sum of the attractive van der Waals potential and the repulsive potential caused by the overlap of the electric double layers[22].

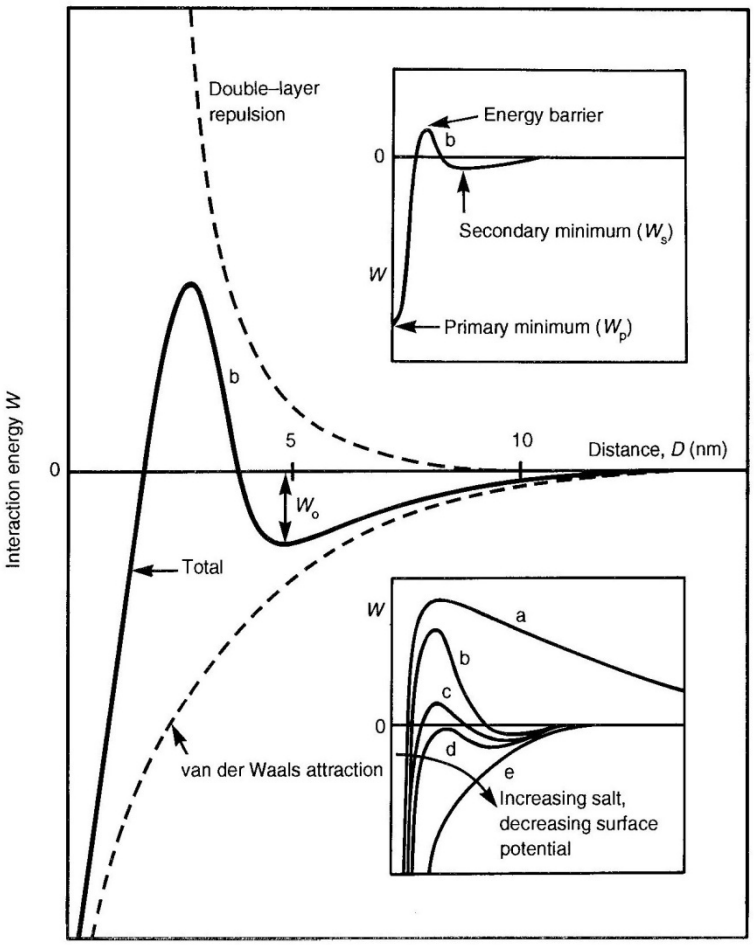

Figure 1.1: DLVO interaction energy as a function of interparticle distance. At low electrolyte concentrations particles repel strongly (a). When increasing the electrolyte concentration a secondary minimum appears in which the particles are aggregated, though the aggregation is reversible (b). A further increase of the electrolyte concentration lowers the energy barrier that prevents the particles from aggregating irreversibly in the primary minimum (c and d), and eventually the barrier disappears whereby the particles aggregate rapidly (e)[22].

As can be observed from Figure 1.1b the DLVO interaction potential may have two minima, namely one when the particles are in contact called the primary minimum and one around 4nm called the secondary minimum. In between the two minima an energy barrier can be observed, which is caused by domination of the repulsive electric double layer term. When particles are in the two minima they are aggregated, and in the primary minimum the aggregation is irreversible, whereas in the secondary minimum it is reversible[22]. The height of the energy barrier, which determines the stability of a colloid dispersion, can be varied by changing the electrolyte concentration in the dispersion medium. An increase in the electrolyte concentration leads to a compression of the electric double layer, illustrated by an increase of κ, whereby W_{elect} and thereby the energy barrier is lowered. Furthermore, an

increased electrolyte concentration lowers the surface potential of the particles, which also lowers W_{elect} , as can be observed from Equation 1.4[18].

1.2.2 Steric Repulsion

Steric stabilization is provided by adsorbed molecules on the particle surface, which sterically repulse similarly adsorbed molecules on other particles. This type of repulsion is not included in the DLVO theory, though if proper molecules are used, this type of repulsion may be very high. To obtain effective steric stabilization the layer of adsorbed molecules must be of sufficient thickness and density to overcome the attractive van der Waals force between the particles[28]. Therefore, the molecules providing the steric stabilization are often polymeric in nature. Steric repulsion between two particles only occurs when the interparticle distance is less than twice the thickness of the adsorbed layer. That is, when the adsorbed layers of the two particles come into physical contact[19]. The steric repulsion is made up of two contributions. One is the unfavourable entropy loss associated with the confinement of the adsorbed molecules when the adsorbed layers of two approaching surfaces start to overlap. The other contribution is osmotic, as the overlap of the adsorbed layers on two surfaces creates a repulsive force due to the increased concentration of adsorbed molecules in the overlap region[22].

1.3 Surface Plasmon Resonance

A metal can be considered as a plasma, which consists of equal concentrations of positive and negative charges with minimum one charge type being mobile[29]. The positively charged metal nuclei are considered immobile, whereas the conduction electrons can be considered as a mobile free-electron gas. Plasmons are quasi-particles of collective oscillations in the free electron charge density, which are enabled by the Coulomb interaction between the valence electrons[30,31].

Surface plasmons are plasmons confined to the interface between two materials. It is required that free electrons are present at the interface, and therefore one of the materials is practically always a metal, such as gold or silver, whereas the other is a dielectric[31]. Surface plasmons may also be interpreted as electromagnetic waves bound to the metal-dielectric surface by interacting with the free electrons of the metal[32]. Two types of surface plasmon resonance exist, namely SPP waves propagating along a metal-dielectric surface, and LSP modes, confined to subwavelength metallic objects[33].

The dispersion relation of the surface plasmons can be deduced from Maxwell's equations, which are stated below[24,34].

$$\nabla \cdot \boldsymbol{B} = 0 \qquad \textbf{Equation 1.5}$$

$$\nabla \cdot \boldsymbol{D} = \rho_f \qquad \textbf{Equation 1.6}$$

$$\nabla \times \boldsymbol{E} = -\frac{\partial \boldsymbol{B}}{\partial t} \qquad \textbf{Equation 1.7}$$

$$\nabla \times \boldsymbol{H} = \boldsymbol{J_f} + \frac{\partial \boldsymbol{D}}{\partial t} \qquad \textbf{Equation 1.8}$$

In the special case where no free charge or free current is found the above equations can be considered as source free, which means that the charge density of free charges, ρ_f, and the current density of free charges, $\boldsymbol{J_f}$, are both equal to zero[35]. In linear isotropic media the

electric field, $\boldsymbol{E}$, and the magnetic field, $\boldsymbol{H}$, are related to the displacement field, $\boldsymbol{D}$, and the magnetic flux density, $\boldsymbol{B}$, as follows[24]:

$$\boldsymbol{D} = \varepsilon\varepsilon_0\boldsymbol{E} \qquad \textbf{Equation 1.9}$$

$$\boldsymbol{B} = \mu\mu_0\boldsymbol{H} \qquad \textbf{Equation 1.10}$$

ε and ε_0 are the relative and the vacuum electric permittivities, respectively, and μ and μ_0 are the relative and the vacuum magnetic permeabilites, respectively. The electric and magnetic fields may be expressed as plane monochromatic waves, which are solutions to Maxwell's equations[24].

$$\boldsymbol{E} = \mathrm{Re}\{\boldsymbol{E}_0 e^{i(\boldsymbol{k}\cdot\boldsymbol{r}-\omega t)}\} \qquad \textbf{Equation 1.11}$$

$$\boldsymbol{H} = \mathrm{Re}\{\boldsymbol{H}_0 e^{i(\boldsymbol{k}\cdot\boldsymbol{r}-\omega t)}\} \qquad \textbf{Equation 1.12}$$

$\boldsymbol{E}_0$ and $\boldsymbol{H}_0$ are the electric and magnetic field amplitudes, respectively, whereas $\boldsymbol{k}$ is the wave vector, $\boldsymbol{r}$ is the position vector, ω is the angular frequency, and t is time. The complex notation of the electric and magnetic fields is mathematically convenient, however to obtain the physical quantities the real parts of the expressions are taken[35]. In the following the "Re" notation is omitted.

1.3.1 Surface Plasmon Polaritons between Semi-Infinite Media

In the simplest case to be considered, surface plasmons propagate at the interface between a semi-infinite metal and a semi-infinite dielectric with electric permittivities $\varepsilon_m(\omega) = \varepsilon_m'(\omega) + i\varepsilon_m''(\omega)$ and $\varepsilon_d = \varepsilon_d' + i\varepsilon_d''$, respectively. Though, ideally ε_d'' is equal to zero. The setup is outlined in Figure 1.2 and a cartesian coordinate system is applied with the x-axis oriented in the surface plasmon propagation direction.

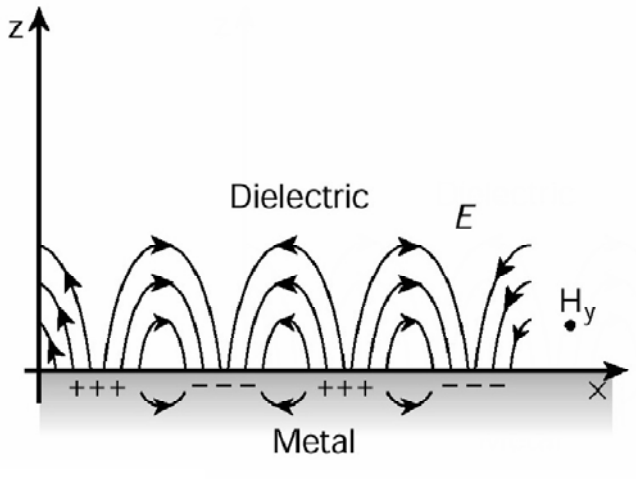

Figure 1.2: Schematic illustration of surface plasmon propagating along the x-axis at metal-dielectric interface between semi-infinite materials[32].

The plane wave solutions to Maxwell's equations can be classified as transverse electric (TE)-polarized or transverse magnetic (TM)-polarized, with the electric or magnetic field parallel to the interface, respectively[30]. However, in order to make waves that propagate

along the metal-dielectric interface the electric field must have a component normal to the interface, meaning that only TM-polarized electromagnetic waves propagate along the interface. When the plasmon waves are TM-polarized the wave vector is $\boldsymbol{k} = (k_x, 0, k_z)$, and the electric and magnetic fields are[32]:

$$\boldsymbol{E}_m = (E_{xm}, 0, E_{zm})e^{i(k_{xm}x - k_{zm}z - \omega t)} \quad z < 0 \qquad \textbf{Equation 1.13}$$

$$\boldsymbol{H}_m = (0, H_{ym}, 0)e^{i(k_{xm}x - k_{zm}z - \omega t)} \qquad \textbf{Equation 1.14}$$

$$\boldsymbol{E}_d = (E_{xd}, 0, E_{zd})e^{i(k_{xm}x + k_{zm}z - \omega t)} \quad z > 0 \qquad \textbf{Equation 1.15}$$

$$\boldsymbol{H}_d = (0, H_{yd}, 0)e^{i(k_{xm}x + k_{zm}z - \omega t)} \qquad \textbf{Equation 1.16}$$

where the subscripts *m* and *d* denotes metal and dielectric, respectively. The fields are restricted to exist at the interface, and decays exponentially as $|z| \to \infty$, which is described by imaginary and positive z-component of the wave vector in the two media[34]. That is, the fields are evanescent in the metal and the dielectric. Introduction of the electric and magnetic fields of Equation 1.13 and Equation 1.14 into Equation 1.8 yields the following:

$$\nabla \times \left\{\left(0, H_{ym}, 0\right)e^{i(k_{xm}x - k_{zm}z - \omega t)}\right\} = \frac{\partial}{\partial t}\left\{\varepsilon_m \varepsilon_0 (E_{xm}, 0, E_{zm})e^{i(k_{xm}x - k_{zm}z - \omega t)}\right\}$$

By considering only the x-component it is found that:

$$-\frac{\partial}{\partial z}\left\{H_{ym}e^{i(k_{xm}x - k_{zm}z - \omega t)}\right\} = \frac{\partial}{\partial t}\left\{\varepsilon_m \varepsilon_0 E_{xm}e^{i(k_{xm}x - k_{zm}z - \omega t)}\right\} \Leftrightarrow$$
$$-H_{ym}k_{zm} = \varepsilon_m \varepsilon_0 E_{xm}\omega \qquad \textbf{Equation 1.17}$$

and

$$H_{yd}k_{zd} = \varepsilon_d \varepsilon_0 E_{xd}\omega \qquad \textbf{Equation 1.18}$$

At the metal-dielectric interface, boundary conditions deduced from Maxwell's equations must be satisfied. The boundary conditions imply that the tangential components of both the electric and magnetic fields must be continuous across the surface, that is at $z = 0$, and this requires both amplitude and phase matching[24]. To obtain amplitude matching it is required that $E_{xm} = E_{xd}$ and $H_{ym} = H_{yd}$. These equalities in combination with Equation 1.17 divided with Equation 1.18 yields the surface plasmon dispersion relation:

$$\frac{-H_{ym}k_{zm}}{H_{yd}k_{zd}} = \frac{\varepsilon_m \varepsilon_0 E_{xm}\omega}{\varepsilon_d \varepsilon_0 E_{xd}\omega} \Leftrightarrow$$
$$\frac{k_{zm}}{k_{zd}} = -\frac{\varepsilon_m}{\varepsilon_d} \qquad \textbf{Equation 1.19}$$

To obtain phase matching at $z = 0$ it is required that $k_{xm} = k_{xd} = k_x$. In non-magnetic, linear, homogeneous, isotropic media the dispersion relation for monochromatic plane waves is[24]:

$$|\boldsymbol{k}| = k = \sqrt{k_x^2 + k_y^2 + k_z^2} = \frac{\omega}{c}\sqrt{\varepsilon} \qquad \textbf{Equation 1.20}$$

with c being the speed of light in vacuum. Hence, in the metal and dielectric, considered in this case, Equation 1.20 yields the following:

$$|\boldsymbol{k_m}|^2 = k_x^2 + k_{zm}^2 = \left(\frac{\omega}{c}\right)^2 \varepsilon_m \qquad \textbf{Equation 1.21}$$

$$|\boldsymbol{k_d}|^2 = k_x^2 + k_{zd}^2 = \left(\frac{\omega}{c}\right)^2 \varepsilon_d \qquad \textbf{Equation 1.22}$$

By combining these two equations with Equation 1.19 another version of the dispersion relation of the surface plasmon propagating at the metal-dielectric interface can be obtained.

$$k_{SP}^{\infty} = k_x = \frac{\omega}{c}\sqrt{\frac{\varepsilon_d \varepsilon_m}{\varepsilon_d + \varepsilon_m}} \qquad \textbf{Equation 1.23}$$

The ∞ implies that the dispersion relation applies to surface plasmons in the semi-infinite case. If damping of the surface plasmon in the x-direction is not accounted for, k_{SP}^{∞} is real, which means that the product and sum of ε_m and ε_d are either both positive or both negative. When considering the interface between a dielectric, which ideally has a real relative permittivity, and a metal, with a complex relative permittivity, k_{SP}^{∞} is also complex. The imaginary component reflects damping of the surface plasmon in the x-direction, and the absorbed energy heats the metal[34,36]. At a gold-water interface, the surface plasmon propagation length, which is the distance at which the energy of the surface plasmon decreases by a factor of $1/e$, is ~17µm when the excitation wavelength is 780nm.

In order to obtain the z-components of the surface plasmon wave vector in the metal and dielectric, Equation 1.23 can be combined with Equation 1.21 or Equation 1.22, respectively, whereby it is found that:

$$k_{zm} = \frac{\omega}{c}\sqrt{\frac{\varepsilon_m^2}{\varepsilon_d + \varepsilon_m}} \qquad \textbf{Equation 1.24}$$

$$k_{zd} = \frac{\omega}{c}\sqrt{\frac{\varepsilon_d^2}{\varepsilon_d + \varepsilon_m}} \qquad \textbf{Equation 1.25}$$

As the z-components of the wave vector are required to be imaginary for the surface plasmon to be confined at the interface it is required that the sum of ε_m and ε_d is negative. Thereby it is also required that the product of ε_m and ε_d is negative, as stated above. Hence, surface plasmons can only exist at interfaces between two media where one medium has a positive real component of the permittivity and the other has a negative real component. Furthermore, it is required that $|\varepsilon_m| > \varepsilon_d$. This applies for dielectrics, which have a positive permittivity, and many metals, such as gold and silver, which have complex permittivity with a negative real component at visible and infrared wavelengths[1,37].

1.3.2 Excitation of Surface Plasmon Polaritons by Light

In order to excite surface plasmons with light, the wave vector of the exciting light wave must be equal to the surface plasmon wave vector at the same angular frequency. As stated in Equation 1.20, the dispersion relation of a plane electromagnetic wave in a homogeneous dielectric with permittivity ε_1 is[32]:

$$k_{ph} = \frac{\omega}{c}\sqrt{\varepsilon_1} \qquad \textbf{Equation 1.26}$$

That is, in the semi-infinite geometry described above SPPs cannot be excited by TM-polarized light from the dielectric side since:

$$k_{ph,x} = \frac{\omega}{c}\sqrt{\varepsilon_d}\sin\theta < \frac{\omega}{c}\sqrt{\frac{\varepsilon_d\varepsilon_m}{\varepsilon_d+\varepsilon_m}} = k_{SP}^{\infty} \qquad \textbf{Equation 1.27}$$

where θ is the angle of incidence of the incoming light. However, this also means that the SPPs do not transform into light, whereby they are non-radiative[32].

In order to circumvent the problem of exciting SPPs the attenuated total reflection (ATR) method may be used. One configuration used for the ATR method is the Kretschmann geometry displayed in Figure 1.3[38].

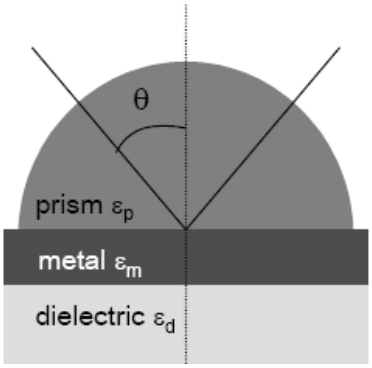

Figure 1.3: Schematic representation of the Kretschmann geometry. A light wave is incident on the prism-metal interface at an angle θ, whereby an evanescent field is created in the metal. The evanescent field is able to excite a surface plasmon on the metal-dielectric interface[32]

With this geometry the SPP is excited at a metal-dielectric interface on one side of a thin metal film by an evanescent field from a metal-prism interface at the opposite side of the metal film. The evanescent field at the metal-prism interface is created by attenuated total reflection. The SPP at the metal-dielectric interface is influenced by the finite thickness of the metal film and the presence of the prism. Therefore the surface plasmon wave vector becomes:

$$k_{SP} = k_{SP}^{\infty} + \Delta k = \frac{\omega}{c}\sqrt{\frac{\varepsilon_d\varepsilon_m}{\varepsilon_d+\varepsilon_m}} + \Delta k \qquad \textbf{Equation 1.28}$$

with k_{SP}^{∞} being the SPP wave vector from the semi-infinite geometry and Δk accounting for the finite thickness of the metal film and the presence of the prism[38]. The prism used in the

Kretschmann geometry is a high refractive index prism with relative electric permittivity $\varepsilon_p > \varepsilon_d$. This enables matching of the wave vector of the incoming light and the SPP wave vector by tuning of ε_p, θ, and the wavelength of the incoming light. That is:

$$k_{ph,x} = \frac{\omega}{c}\sqrt{\varepsilon_p}\sin\theta_{SP} = \frac{\omega}{c}\sqrt{\frac{\varepsilon_d\varepsilon_m}{\varepsilon_d+\varepsilon_m}} + \Delta k = k_{SP} \qquad \textbf{Equation 1.29}$$

The dispersion relations of a photon in the dielectric, a photon in the prism, and surface plasmon are shown in Figure 1.4. The resonance condition is fulfilled where the dispersion relations intersect.

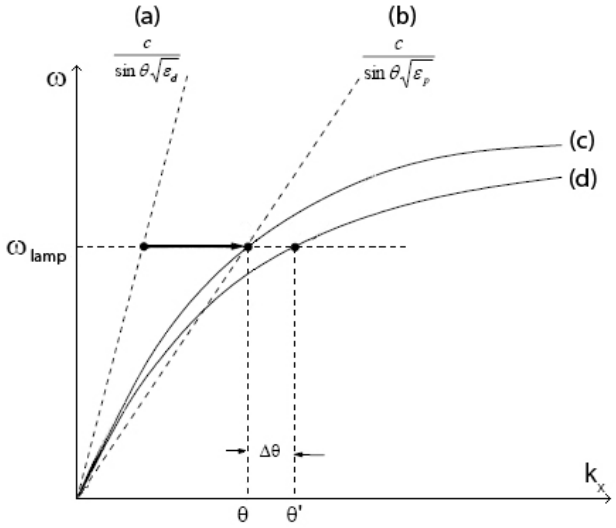

Figure 1.4: Dispersion relations of photons in a dielectric (a) and in a prism (b) at angle of incidence θ, and surface plasmon dispersion relation (c). The dispersion relation of the surface plasmon at increased permittivity of the dielectric is shown in (d)[32].

As can be observed in the figure, the dispersion relations only intersect at one point, which means that at a certain wavelength only one resonance angle exists. This resonance condition is observed as a decrease in reflectivity from the prism-metal interface[34]. In Figure 1.5 the reflectivity as a function of angle of incidence of the incoming light at constant wavelength can be observed. The reflectivity as a function of wavelength at constant θ would show a similar dip in reflectivity[38]. Furthermore, it appears from the figure how the reflectivity is affected by the metal film thickness. Though it might be expected that the reflectivity is equal to unity at conditions where no surface plasmons are excited, this is not the case. The reflectivity is never equal to unity due to an energy loss of the ATR-generated evanescent field in the metal, which is described by the complex permittivity of the metal[35,39].

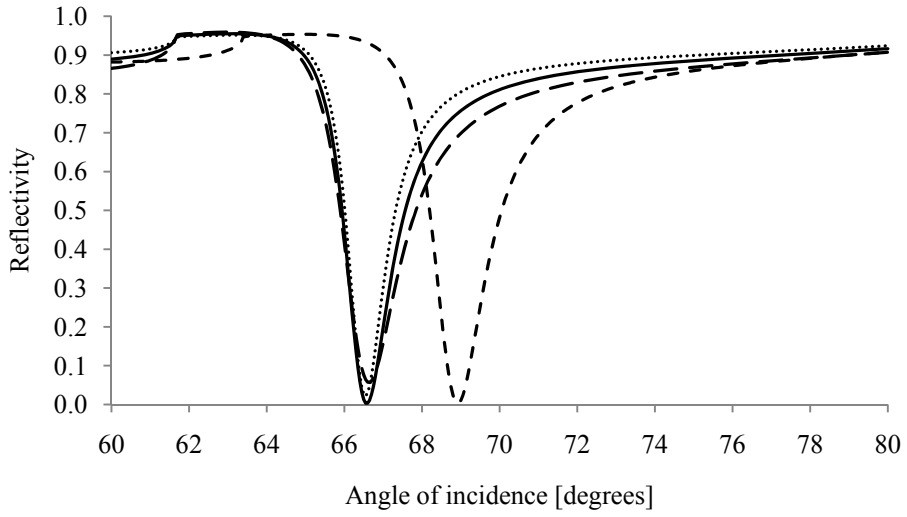

Figure 1.5: Reflectivity as function of the angle of incidence of TM-polarized light with a wavelength of 780nm. The configuration is glass (ε_p = 2.280), gold film (ε_m = -22.5+1.40*i*), dielectric (ε_d = 1.766), with film thickness of 45nm (long dashed line), 50nm (solid line), and 55nm (dotted line). Furthermore, the reflectivity is plotted with an increased dielectric permittivity (ε_d = 1.823) and a film thickness of 50nm (short dashed line)[34,38].

1.3.3 Surface Plasmon Resonance for Sensing

The surface plasmon resonance condition is sensitive to changes in the permittivity of the dielectric, as is evident from Equation 1.23. However, as the field of the SPP in the dielectric is evanescent, and therefore decays exponentially, it is highly sensitive to changes in the permittivity in the vicinity of the metal-dielectric interface and less sensitive further away from the interface[32]. The change in permittivity may be monitored as a change in the SPP resonance angle at constant wavelength, or a change in resonance wavelength at constant angle. It can be observed from Figure 1.5, that at constant wavelength an increase in the dielectric permittivity entails an increase in the resonance angle. Similarly, at constant angle the resonance wavelength increases when the dielectric permittivity increases.

Binding of molecules, such as DNA or proteins, at the metal surface changes the permittivity, and the concentration of molecules on the surface is directly correlated to the change in resonance angle[32]. Thereby it is possible to detect binding of molecules at the metal surface.

1.3.4 Localized Surface Plasmons

In contrary to the propagating SPPs, LSPs are non-propagating excitations of the free conduction electrons of subwavelength metallic nanoparticles coupled to an electromagnetic field[1]. The curved surface of the nanoparticles subjects the electrons to an effective restoring force, whereby a resonance condition arises. Furthermore, the curved surface permits direct excitation of the LSPs by light, in contrary to the SPPs, which requires e.g. ATR illumination for excitation[1]. Excitation of LSPs by light leads to strong scattering and absorption of the light. For spherical silver and gold nanoparticles the resonance conditions are satisfied at visible wavelengths[40].

The phenomenon of LSPs can be theoretically described by the Mie theory as a summation over all electric and magnetic multipole oscillations[41]. However, when the metal

nanoparticle is spherical with a diameter more than ten times smaller than the wavelength of the exciting light only the dipole term in the summation is significant[10]. For a particle immersed in a dielectric medium the extinction cross section, which is the sum of the absorption and scattering cross sections, is then[41]:

$$\sigma_{ext} = 9\frac{\omega}{c}V\varepsilon_d^{3/2}\frac{\varepsilon_m''}{(\varepsilon_m' + 2\varepsilon_d)^2 + \varepsilon_m''^2} \qquad \textbf{Equation 1.30}$$

where V is the volume of the spherical particle. From this equation it is observed that the resonance condition is satisfied when $\varepsilon_m' \approx -2\varepsilon_d$ when e_m'' is only weakly dependent on the angular frequency. The fact that the resonance condition depends on the permittivity of the dielectric surrounding the nanoparticle is very convenient, as the binding of e.g. DNA at the nanoparticle surface increases the permittivity. The permittivity of Ag and Au decreases at increasing wavelengths and therefore the resonance wavelength is increased at binding of the DNA[42]. Hence, the binding can be monitored by measuring the extinction of a nanoparticle solution, as exemplified in Figure 1.6 where spectra of Ag nanoparticles and DNA-Ag nanoparticle conjugates are depicted.

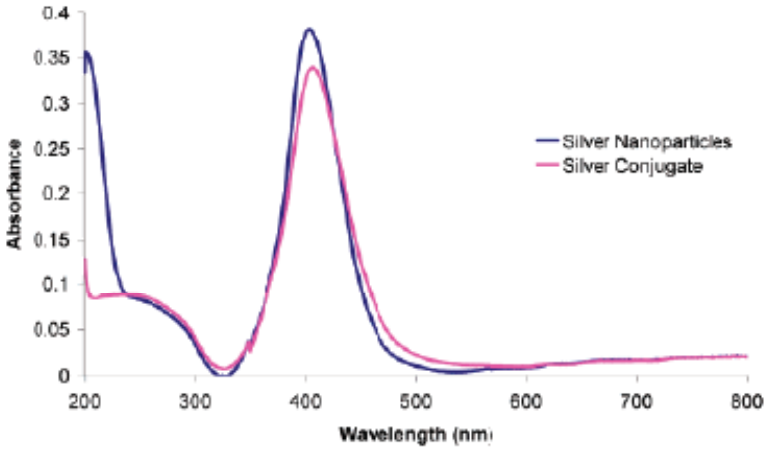

Figure 1.6: Absorance spectra of Ag nanoparticles (Silver Nanoparticles) and DNA-Ag nanoparticle conjugates (Silver Conjugate)[12].

Furthermore, the resonance condition depends on the size of the nanoparticle. This is entailed by the fact that the permittivity of the metal nanoparticle is dependent on the collisions of the free electrons with the particle boundary, whereby it becomes size dependent and different from the permittivity of bulk metal[40]. The width of the resonance band is determined by e_m'', which is the reason why silver, which has a smaller imaginary component than gold, exhibits a sharper resonance peak. However, the width also depends on particle size and on the presence of adsorbed molecules on the nanoparticle surface[10,41,43].

The LSP resonance condition of a metal nanoparticle is also influenced by the presence of other nearby nanoparticles, as the LSPs in the particles are able to couple. When coupling occurs the plasmon resonance is red-shifted and the resonance band is broadened[42]. The change is caused by a change in the electromagnetic field experienced by the nanoparticle, as the experienced field consists of both the incident light and the light scattered by the nearby particle. The magnitude of the red-shift of the plasmon resonance

depends on the strength of the interparticle coupling, which depends on the distance between the nanoparticles. According to Jain *et al* (2007), the red-shift, $\Delta\lambda$, decays approximately exponentially with interparticle distance, *s*, as is depicted in the following empirical equation[11]:

$$\frac{\Delta\lambda}{\lambda_0} = a \cdot e^{\frac{-s/D}{b}}$$ **Equation 1.31**

λ_0 is the single-particle plasmon wavelength maximum, *D* is the particle diameter, and *a* and *b* are constants. The magnitude of the plasmon shift illustrated by *a* is larger for Ag nanoparticles than for Au nanoparticles due to the fact that the electromagnetic fields are stronger in a Ag nanoparticle system[11]. The red-shifting resonance peak is attributed to dipolar interactions between the nanoparticles. However, at very small interparticle separations an additional peak appears, which may be attributed to quadropolar resonances[44].

1.3.5 Coupling of Surface Plasmon Polaritons and Localized Surface Plasmons

Coupling is also possible between LSPs and SPPs. When a nanoparticle is positioned above a thin metal film the LSP of the nanoparticle and the thin film SPP interact[15]. The interaction is particularly strong when the nanoparticle-film distance is less than ~50nm[15]. This type of system with a gold nanoparticle bound at different distances above a thin gold film has been studied experimentally by Mock *et al.*[15] and theoretically by Leveque and Martin[33,45]. With white light excitation at constant angle of incidence using Kretschmann geometry, Leveque and Martin found that the SPP resonance wavelength was essentially not displaced when the nanoparticle-film distance was larger than 100nm. In contrary, the LSP resonance wavelength of the nanoparticle was found to start red-shifting when the distance between the metal film and the nanoparticle was below 50nm. The red-shift increased when the metal film-nanoparticle distance was further decreased[45].

In the study of Mock *et al.* the system was created by binding of a spherical 60nm gold nanoparticle to a polyelectrolyte layer on top of a 45nm gold film on a prism. The thickness *d* of the polyelectrolyte layer was varied between 0.64 and 22.3nm, and two different approaches were used to excite the system, as shown in Figure 1.7. One approach was excitation of the LSP of the nanoparticle with dark-field illumination, as illustrated in Figure 1.7a.

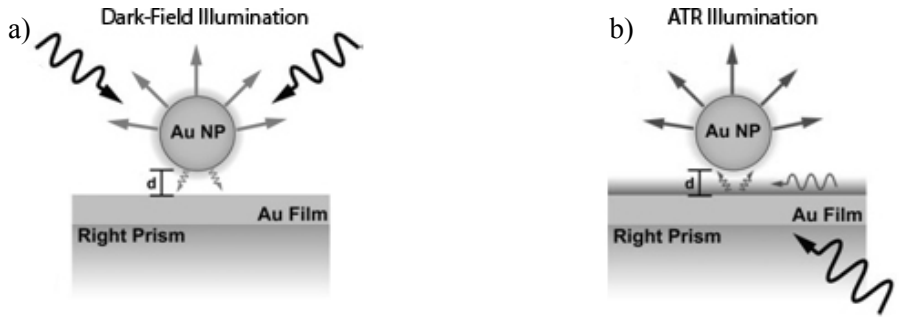

Figure 1.7: Illumination schemes used by Mock *et al.* a) White light dark-field illumination. b) White light ATR excitation with TM-polarized at 45° angle of incidence[15].

With this approach only the LSP of the nanoparticle is directly excited by the light, whereas the light cannot couple with the SPP due to mismatch of the wave vectors. However, the white light scattered by the nanoparticle couples with the whole continuum of SPPs in the gold film. In Figure 1.8a images and scattering spectra of single nanoparticles excited by dark-field illumination with variable distance between nanoparticle and metal film are displayed. Since no particular SPP mode is excited with this illumination scheme the spectra are dominated by the LSP resonance, which is observed to red-shift when the distance between the nanoparticle and the metal film is decreased. The LSP resonance might be expected to be influenced by the altered permittivity caused by the presence of the polyelectrolyte layer between the nanoparticle and the metal film[33]. However, this effect appears small compared to the coupling interaction between nanoparticle and metal film[15].

Another illumination scheme used was ATR illumination, wherein excitation with white light at a 45° angle of incidence with Kretschmann geometry was established, and thereby an evanescent wave was produced. With this approach the evanescent wave excites a single SPP mode in the metal film, which is then able to couple with the nanoparticle, thereby allowing scattering of the light by the nanoparticle. Furthermore, the LSP of the nanoparticle is directly excited by the evanescent wave. Images and scattering spectra from single nanoparticles obtained with this illumination scheme are shown in Figure 1.8b. These spectra are influenced by two contributions. One contribution is the red-shift of the LSP at decreasing separation between nanoparticle and metal film, as was observed with dark-field illumination, whereas the other contribution originates from the single SPP mode scattered by the nanoparticle. The SPP is influenced by the presence of the polyelectrolyte layer, which causes a red-shift of the SPP mode at increasing thickness. That is, the observed scattering spectra are influenced by a red-shifting LSP mode and a blue-shifting SPP mode at decreasing separation[15].

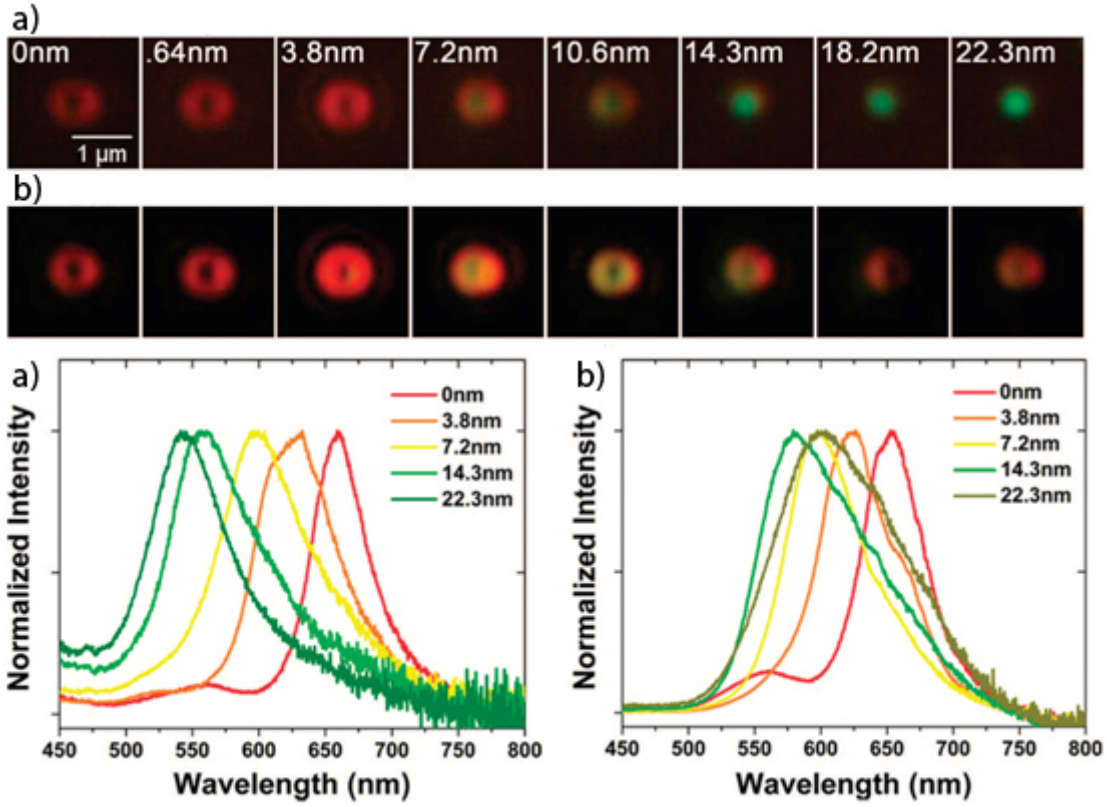

Figure 1.8: Scattering images and spectra of 60nm gold nanoparticles at increasing separation provided by polyelectrolyte above gold film. a) Single nanoparticles illuminated according to dark-field scheme. b) Single nanoparticles illuminated according to ATR scheme[15].

1.4 Indolicidin

Cationic antimicrobial peptides have been isolated from a wide range of organisms including mammals, and they are part of the innate host defense system[46]. IL belongs to this class of peptides and it has the amino acid sequence ILPWKWPWWPWRR-NH_2 [47]. It was discovered from the cytoplasmic granules of bovine neutrophils, and the short sequence makes it the smallest of the known naturally occurring linear antimicrobial peptides[46]. The structure of IL is unordered in aqueous medium[48]. There have been reports on antibacterial, antifungal, antiparasitic, and antiviral functions of IL[47]. However, its mechanism of action is not completely determined[49]. It has been shown that IL works by binding to and permeabilizing cell membranes though without lysing the cells[50,51]. Additionally it is able to inhibit DNA synthesis in Escherichia coli[51]. Other studies have shown that IL is able to bind DNA, which may be part of the IL mechanism of action[46,47].

The antimicrobial properties of IL make it interesting as an alternative for antibiotics. This potential use of IL is however complicated by the fact that the peptide is relatively toxic toward mammalian cells[52]. IL has been reported to cause lysis of erythrocytes and display cytotoxicity towards human lymphocytes. In contrary, single tryptophan analogs of IL synthesized by Subbalakshmi *et al.* (2000) exhibit no hemolytic activity, whereas the antibacterial activity of the analogs is retained, though at a lower potency[48]. The analogs were constructed with the 4^{th} (IL-4) 8^{th} (IL-8), or 11^{th} (IL-11) tryptophan retained and the remaining tryptophans substituted by leucines.

2 Materials and Methods

This section contains a description of methods used for stabilization of Ag nanoparticles with ATP, pto-ATP, and following conjugation with DNA. Furthermore, a method used for conjugation and stabilization of Ag nanoparticles in one step by use of four different DNA strands is described. A method for linking of the DNA protected Ag nanoparticles or dsDNA to Au surfaces and further linking of IL-4 to the dsDNA or the DNA interlinking the Au surface and the Ag nanoparticles is also presented. The techniques used for examination of the produced structures are described.

The chemicals used for the experiments are listed in Appendix A.

2.1 DNA

Single stranded DNA (ssDNA) with the sequences listed in Table 2.1 was ordered from Eurofins MWG Operon. The DNA was prepared in aliquots containing 1nmole by dissolving DNA stocks in sterilized MilliQ water, separating the DNA into aliquots, and finally freeze drying for storage at -20°C.

DNA Sequence	Abbreviation
5'-CTT GAT GCA ATA TTA ACC ATG TCC CGT TTG-3'	r-DNA
5'-HOC_6S-SC_6-CCC CCC CCC CCC CCC CCC CCC CCC CT*T* T*T*T* T*T*T* T*T*G GGG GGG GGG GGG GGG GGG GGG GGG-3'	hp-DNA
5'-FAM-CCC CCC CCC CCC CCC CCC CCC CCC CT*T* T*T*T* T*T*T* T*T*G GGG GGG GGG GGG GGG GGG GGG GGG-3'	FAM-hp-DNA
5'-C*C*C* C*C*C* C*C*C* C*AA AAA ACA CAC ACA CAA AAA-3'	pto-DNA
5'-HOC_6S-SC_6-TTT TTT GTG TGT GTG TTT TT-3'	thiol-DNA

Table 2.1: Sequences of DNA strands used for experiments. HOC_6S-SC_6 designates a 5' disulphide bridge linked to the DNA with a hexane linker, whereas * marks bases with a phosphorothioated backbone and FAM designates the presence of a FAM fluorophore. Bases forming a loop region in hairpin forming DNA strands are underlined.

2.2 Software Analysis of DNA Structures

The ability of the sequences of r-DNA, hp-DNA, FAM-hp-DNA, pto-DNA, and thiol-DNA to form secondary structures and homo-dimers was examined using OligoAnalyzer 3.1 from INTEGRATED DNA TECHNOLOGIES[53]. Furthermore, the ability of pto-DNA and thiol-DNA to form hetero-dimers was examined. The following settings were used when utilizing the Self-Dimer and Hetero-Dimer functions: Target Type: DNA; Oligo Conc: 1μM; Na^+ Conc: 20mM; Mg^{++} Conc: 0mM; dNTPs Conc: 0mM. The Hairpin function was used with the following settings: Nucleotide Type: DNA; Sequence Type: Linear; Temperature: 20°C; Suboptimality: 50%; Sodium Concentration: 20mM; Magnesium Concentration: 0mM.

2.3 Preparation of Ag Nanoparticles

Ag nanoparticles were synthesized from solutions of 30ml 1mM $NaBH_4$ in MilliQ water and 10ml 1mM $AgNO_3$ in MilliQ water. Both solutions were cooled on ice before the $NaBH_4$ solution was added to the $AgNO_3$ solution while stirring. The mixture was not exposed to light and cooled on ice while stirring for 2h.

2.3.1 Stabilization of Ag Nanoparticles with ATP or pto-ATP

Stabilization of Ag nanoparticles was attempted with a final concentration of 100µM ATP or pto-ATP, which was added during or after the nanoparticle synthesis. When added during the synthesis, ATP or pto-ATP was added to the $AgNO_3$ solution immediately before addition of $NaBH_4$, whereas addition after the synthesis was done by adding the ATP or pto-ATP immediately after the synthesis. When the stabilizing agents were added after the synthesis the solutions were left for incubation at room temperature for 2h.

2.3.2 Binding of hp-DNA to ATP or pto-ATP Stabilized Ag Nanoparticles

In order to be able to bind the ATP or pto-ATP stabilized Ag nanoparticles to a gold surface, binding of DNA to the stabilized particles was necessary. Therefore it was attempted to bind hp-DNA to the nanoparticles. In advance, the disulphide bridge at the 5' end of the DNA was cleaved with dithiothreitol (DTT) to create a free thiol, and the hairpin structure was temporarily unfolded by increasing the pH with NaOH. The DTT was added at a concentration of 100mM to 11.1µM hp-DNA in 10mM Tris-1mM EDTA (TE) buffer pH 8.5 followed by 30min incubation at room temperature. Thereafter NaOH was added for a final concentration of 100mM whereby the DNA concentration was changed to 10µM. The DTT was removed and the pH was lowered again by use of illustra NAP-5 column (GE Healthcare, Little Chalfont, UK). The column was equilibrated with 2mM Tris-HCl buffer pH 7.5 and the DNA solution was desalted as prescribed by the manufacturer. After desalting, the DNA concentration was expected to be 2µM.

Samples were then prepared containing 500µl of bare, ATP stabilized, or pto-ATP stabilized Ag nanoparticles, to which 200µl 2µM hp-DNA was added. Furthermore, reference samples without DNA were prepared containing 200µl 2mM Tris-HCl buffer pH 7.5 instead of DNA. Afterwards, NaCl was added to the samples for a final concentration of 10mM followed by 1h incubation at room temperature. This was succeeded by another NaCl addition for a final NaCl concentration of 20mM. Lastly, the samples were left for overnight incubation at room temperature.

2.3.3 Stabilization of Ag Nanoparticles with DNA

For production of DNA stabilized Ag nanoparticles, synthesis of the particles was performed as described above. However, 26.67mM NaCl was present in the $NaBH_4$ solution, whereby the final concentration of NaCl in the Ag nanoparticle solution became 20mM. Two series of samples were made containing the newly synthesized Ag nanoparticles and r-DNA, hp-DNA, FAM-hp-DNA, or pto-DNA. One series contained 1.43µM DNA whereas the other contained 2.86µM DNA. Furthermore, a sample containing Ag nanoparticles and 28.6µM ATP was prepared. The samples were incubated in dark at 60°C for 2h, whereafter they were further incubated at room temperature overnight.

2.4 Binding of pto-DNA Stabilized Ag Nanoparticles to Au Surface

In order to be able to image the assay used in the SPR experiments by AFM the Ag nanoparticles stabilized with pto-DNA were bound to a flame annealed Au surface (arrandee™, Werther, Germany) or an Au surface of the type used for SPR experiments (XanTec Bioanalytics, Lotnr.: SC AU 12 07 P4). 10µM thiol-DNA was deprotected with 100mM DTT dissolved in 400mM Tris-HCl pH 7.5 for 30min. Afterwards the DTT was removed by running the sample through two illustra NAP-5 columns (GE Healthcare, Little Chalfont, UK). The columns were equilibrated with 400mM Tris-HCl pH 7.5, and the DNA was eluted as prescribed by the manufacturer. After removal of DTT the DNA concentration was expected to be 1µM. The deprotected thiol-DNA was placed in a drop on a newly flame annealed Au surface, which was then incubated for 2h at room temperature in a humidity chamber to avoid evaporation of the droplet. Following, excess DNA was flushed off the surface with 10ml MilliQ water, and the surface was placed in 1mM mercaptohexanol dissolved in MilliQ water for 1 hour. Excess mercaptohexanol was removed by flushing with 30ml MilliQ water, whereafter the surface was blow dried with nitrogen. Ag nanoparticles stabilized with 1.43µM pto-DNA were prepared by centrifugation at 12000g for 10min at 20°C in order to remove excess DNA and concentrate the nanoparticles. The pellet from the centrifugation containing the Ag nanoparticles was then dispersed in 40% of the initial volume in 2mM Tris-HCl pH 7.5 containing 500mM NaCl. The concentrated Ag nanoparticles stabilized with pto-DNA were then placed in a drop on the surface and incubated overnight in a humidity chamber at room temperature. Hereafter, the surface was flushed with 30ml MilliQ water, blow dried with nitrogen, and imaged by AFM.

2.5 UV-Vis Absorbance Spectroscopy

The absorbance spectra of Ag nanoparticles were measured using a VWR International UV-1 UV-Vis spectrophotometer in the wavelength range 250-800nm. The spectra were measured with a wavelength resolution of 1nm and UV cuvettes with a light path length of 1cm were used.

2.6 Gel Electrophoresis

The mobility of DNA stabilized Ag nanoparticles was examined in 1% agarose gel at 50V applied for 60min. 1X tris-borate EDTA (TBE) buffer was used as running buffer. Samples were prepared by concentrating the samples by centrifugation at 12000g for 10min at 20°C and resuspending them in a volume 3% of the initial volume. Loading buffer (10mM EDTA, 50% (v/v) glycerol) pH 8.5 was added to the samples in the ratio 1:6. The gel was stained with ethidium bromide.

2.7 Atomic Force Microscopy

Atomic force microscopy images of the samples produced as described in Section 2.4 and of hp-DNA stabilized Ag nanoparticles deposited on a flame annealed Au surface were obtained in air at room temperature. Deposition of hp-DNA stabilized Ag nanoparticles was done by placing a droplet of Ag nanoparticles with 2.86µM hp-DNA on the flame annealed Au surface. The sample was afterwards incubated at room temperature in a humidity

chamber for 2 days. Before imaging with AFM, the Au surface was flushed with 2ml MilliQ water and blow dried with nitrogen.

The AFM used was a Digital Instruments Multimode Nanoscope IIIa AFM from Veeco operated in tapping mode on. The microscope was equipped with a "J" scanner and OMCL-AC160TS cantilevers from Olympus (k = 42N/m, f = 300kHz). The microscope was controlled with Nanoscope software version 530r3sr3. The captured images were plan subtracted and flattened using the Nanoscope software, and otherwise processed using WSxM 5.0 Develop 1.0 software[54].

2.8 Fast Protein Liquid Chromatography

Purification of IL-4 was done by use of fast protein liquid chromatography (FPLC). IL-4 was kindly provided by associate professor P. Fojan. The peptide was synthesized by use of Fmoc solid-phase peptide synthesis. For purification, the synthesis product was resuspended in 5% (v/v) TFA in MilliQ water at a concentration of 1.5mg/ml. The suspension was purified using FPLC on an ÄKTApurifier 10/100 (GE Healthcare) with a Superdex Peptide 10/300 column (GE Healthcare) equilibrated with 0.1% (v/v) formic acid. The flow rate was 0.5ml/min and the eluted sample was fractionized and characterized by measuring conductivity and absorbance at wavelengths of 215nm, 254nm, and 280nm. The fractionized samples were freeze-dried and stored at -20°C until they were further used. For further use, the IL-4 concentration was calculated from a molar extinction coefficient of 5690$cm^{-1}M^{-1}$ at 280nm[55].

2.9 Surface Plasmon Resonance Spectroscopy

Binding of IL-4 to dsDNA was monitored by SPR spectroscopy with and without Ag nanoparticles linked to the DNA. SPR measurements were performed on a Reichert SR7000DC instrument (Reichert, Depew, NY) controlled by Reichert SPR V.4.0.17 software. The system was configured with the two cell chambers connected in series with the flow entering the left chamber first. The left and right chambers are subsequently designated as sample and reference chambers, respectively. Flow was maintained with a Harvard Apparatus PHD 2000 Programmable syringe pump and the flow rate was 10µl/min unless anything else is stated. The temperature was set at 25°C, and bare Au surface sensor chips produced in house were used for all experiments. The chips were cleaned in an ozone cleaner from BIOFORCE Nanosciences, model UV.TC.EU.003 for 30min prior to mounting in the SPR instrument. The SPR instrument was calibrated following the manufacturer recommendations for the produced chips with ethylene glycol.

When mounted in the instrument the Au surface was equilibrated with 2mM Tris-HCl buffer pH 7.5, which was used as running buffer. Several injections of 99% EtOH were made in order to rinse the surface. After proper rinsing, the system was rewired to establish flow through the sample chamber only, whereafter deprotected thiol-DNA with an expected concentration of 870nM was injected. The thiol-DNA was deprotected as described in Section 2.4 and it was hence dissolved in 400mM Tris-HCl buffer pH 7.5. 20min after the injection was started the flow rate was decreased to 2µl/min for 100min to allow binding of thiol-DNA to the Au surface. Following, the injection was stopped and the flow rate was increased to 10µl/min. When excess DNA had been washed off the surface the system was

rewired to establish flow in both chambers, though this time with the flow entering the reference chamber first. This was followed by 20min injection of 1mM mercaptohexanol dissolved in MilliQ water. Hereafter, the flow rate was decreased to 2µl/min for 40min and then the injection was stopped and the flow rate was again set to 10µl/min. In order to obtain dsDNA on the surface, Ag nanoparticles stabilized with 1.43µM pto-DNA or pure pto-DNA, which is complementary to thiol-DNA, was injected. Pto-DNA was injected at a concentration of 870nM, whereas the Ag nanoparticles were prepared as described in Section 2.4. Both pto-DNA and Ag nanoparticles were dissolved in 2mM Tris-HCl buffer pH 7.5 containing 500mM NaCl, and binding to the surface was done by injecting either of the samples into both chambers and then stopping the flow for 1h. Prior to the injections of DNA, mercaptohexanol, and IL-4, 10min injections of the buffers wherein they were dissolved were made.

Different concentrations of IL-4 dissolved in 2mM Tris-HCl buffer pH 7.5 were flushed over the dsDNA covered Au surface in 1h injections. The surface was regenerated with 500mM NaCl in 2mM Tris-HCl pH 7.5 between each IL-4 injection. Binding kinetics of IL-4 binding to dsDNA was evaluated using Scrubber2 software version 2.0b from BioLogic Software. Binding curves were produced by subtracting the reference chamber response from the sample chamber response. Reflectivity scans, with the reflectivity of the two channels measured as a function of the angle of the light exciting the surface plasmons, were measured before and after the pto-DNA or pto-DNA modified Ag nanoparticle injection and after the second IL-4 injection. The reflectivity scans were normalized with a scan obtained with air in the sample and reference chambers.

3 Results

Stabilization of Ag nanoparticles was attempted with the use of the mononucleotides ATP and pto-ATP, and furthermore binding of phosphorothioated hairpin DNA to these particles was attempted. The effect of phosphorothioated DNA, or unmodified DNA as stabilizing agents for Ag nanoparticles was also investigated. The stabilizing effect of the agents was monitored by absorbance spectroscopy and agarose gel electrophoresis, and the ability of the used DNA sequences to form secondary structures and homo- or hetero-dimers was determined by software analysis.

Binding of IL-4 to dsDNA bound to an Au surface and dsDNA interlinking an Au surface and Ag nanoparticles was monitored with SPR spectroscopy. The linking of hp- or pto-DNA modified Ag nanoparticles to the Au surface was investigated using AFM imaging in order to determine the most appropriate method for production of the SPR assay.

3.1 Software Analysis of DNA Structures

The ability of the DNA strands presented in Section 2.2 to form secondary structures and homo-dimers was examined using OligoAnalyzer 3.1. However, the 5' and internal modifications of the DNA strands was not included in the calculations. It was found that the most stable secondary structure formed by r-DNA has a melting temperature (Tm) of 13.5°C with a Gibbs free energy increment (ΔG) of 0.87kcal/mole. The secondary structure may be observed in Figure 3.1 along with the most stable homo-dimer formed by r-DNA, which is linked by six consecutive base pairs and has a ΔG of -7.8kcal/mole.

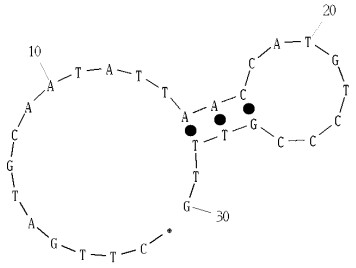


```
5'          CTTGATGCAATATTAACCATGTCCCGTTTG
                          ||||||
3' GTTTGCCCTGTACCAATTATAACGTAGTTC
```

Figure 3.1: Most stable secondary structure (left) and most stable homo-dimer (right) formed by r-DNA[53].

The most stable secondary structure formed by hp-DNA and FAM-hp-DNA is depicted in Figure 3.2. The folding of this structure results in a ΔG of -36.54kcal/mole, and this entails a Tm of 92.7°C. Additionally, the most stable homo-dimer, formed by 25 consecutive base pairs in each end, is depicted in the figure. The ΔG of the homo-dimer formation is -73.66kcal/mole.

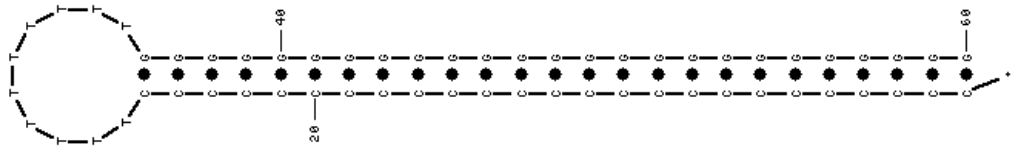

```
5' CCCCCCCCCCCCCCCCCCCCCCCCCTTTTTTTTTTGGGGGGGGGGGGGGGGGGGGGGGG
   |||||||||||||||||||||||||          ||||||||||||||||||||||||||
3' GGGGGGGGGGGGGGGGGGGGGGGGGTTTTTTTTTTCCCCCCCCCCCCCCCCCCCCCCCC
```

Figure 3.2: Most stable secondary structure (top) and most stable homo-dimer (bottom) formed by hp-DNA and FAM-hp-DNA[53].

The analysis of pto- and thiol-DNA showed that neither of the two sequences are able to form secondary structures or homo-dimers. Though, they are able to form hetero-dimers with the most stable form having a ΔG of -32.03kcal/mole, as illustrated in Figure 3.3.

```
5' CCCCCCCCCCAAAAAACACACACACAAAAA     (pto-DNA)
             ||||||||||||||||||
3'           TTTTTGTGTGTGTTTTTT     (thiol-DNA)
```

Figure 3.3: The most stable hetero-dimer formed by pto- and thiol-DNA[53].

3.2 Absorbance Spectra of Ag Nanoparticles

The band position and bandwidth of nanoparticle LSPs is determined by the nanoparticle size and the presence of adsorbed molecules at the nanoparticle surface, as described in Section 1.3.4. In the free-electron limit the LSP extinction band of metals can be fitted to a Lorentzian curve[43]. Therefore, the measured absorbance spectra of Ag nanoparticles have been fitted to Lorentzian curves to determine the plasmon band full width at half maximum (FWHM) and, when possible, also the wavelength of maximum absorbance (λ_{max})[41]. The LSP band of unmodified Ag nanoparticles is situated around 400nm.

3.2.1 Stabilization of Ag Nanoparticles with ATP or pto-ATP

Based on the fact that ATP may be used for stabilization of Au nanoparticles, this was also attempted with Ag nanoparticles[56]. Furthermore, phosphorothioated DNA residues have been shown to interact specifically with Ag nanoparticles, wherefore it was also attempted to stabilize Ag nanoparticles with pto-ATP[57]. Absorbance spectra of Ag nanoparticles stabilized with ATP or pto-ATP added during or after the nanoparticle synthesis, as described in Section 2.3.1, are shown in Figure 3.4.

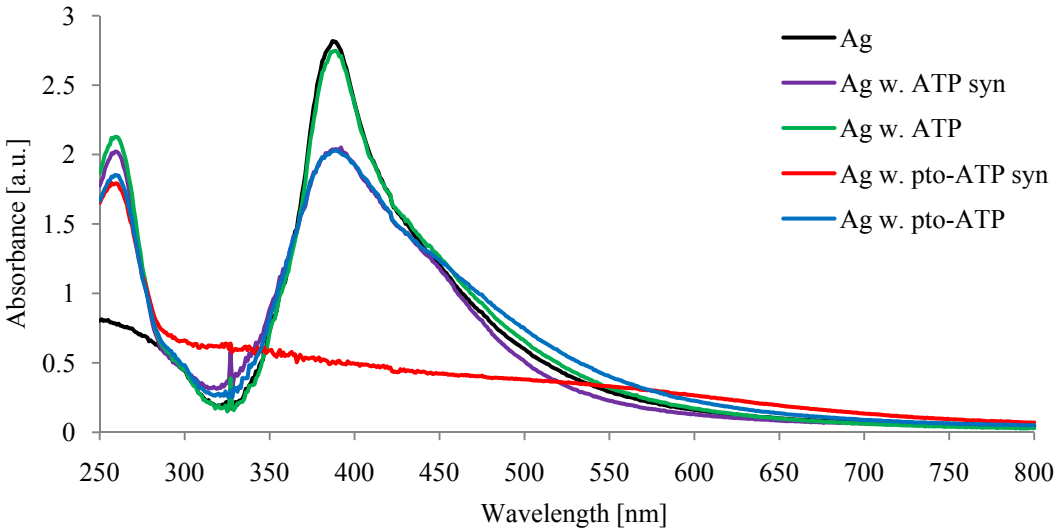

Figure 3.4: Absorbance spectra measured on the day of synthesis of bare Ag nanoparticles (Ag), Ag nanoparticles with ATP added during (Ag w. ATP syn) or after (Ag w. ATP) the synthesis, or with pto-ATP added during (Ag w. pto-ATP syn) or after (Ag w. pto-ATP) the synthesis. The x- and y-axis represent absorbance wavelength in nm and absorbance, respectively.

The λ_{max} and FWHM of the LSP bands determined by fitting a Lorentzian curve to the absorbance spectra in Figure 3.4 are found in Table 3.1.

Sample		λ_{max} [nm]	Intensity at λ_{max}	FWHM [nm]	R^2
Ag		387	2.817	115.1±1.2	0.99002
-||-	1 day	387	2.878	107.4±1.0	0.99191
-||-	2 days	389	2.914	99.1±0.9	0.99185
-||-	3 days	388	2.997	92.8±0.7	0.99406
-||-	7 days	390	3.155	84.2±0.7	0.99433
-||-	44 days	392.3±0.2	3.167	71.5±0.6	0.99605
Ag w. ATP syn		389.3±0.5	2.039	138.6±1.3	0.99679
-||-	1 day	393	2.363	99.8±1.0	0.99191
-||-	2 days	395	2.419	89.9±0.8	0.99304
-||-	3 days	395	2.491	80.8±0.7	0.99310
-||-	7 days	398.5±0.2	2.529	72.6±0.6	0.99543
-||-	44 days	399.8±0.1	2.536	66.8±0.5	0.99663
Ag w. ATP		389	2.747	125.1±1.5	0.98678
-||-	1 day	389	2.741	124.7±1.5	0.98644
-||-	2 days	389	2.772	124.2±1.5	0.98631
-||-	3 days	386	2.700	129.1±1.4	0.98875
-||-	7 days	388	2.718	126.0±1.5	0.98646
-||-	44 days	388	2.476	119.6±1.3	0.98872
Ag w. pto-ATP syn		-	-	-	-
Ag w. pto-ATP		388	2.031	175.8±1.1	0.99617
-||-	1 day	389	1.976	180.2±1.1	0.99648
-||-	2 days	389	1.848	193.4±1.1	0.99723
-||-	3 days	406	1.407	246.4±1.6	0.99671
-||-	7 days	416.6±0.6	1.198	294.9±2.4	0.99794
-||-	44 days	405	0.847	399.9±3.1	0.99607

Table 3.1: Wavelength of maximum absorbance (λ_{max}) and full width at half maximum (FWHM) of the LSP band deduced from the spectra in Figure 3.4-Figure 3.7. When no uncertainty is stated λ_{max} is read from the absorbance spectra, whereas FWHM and λ_{max} with uncertainties stated were obtained by fitting a Lorentzian curve to the absorption peak from the data between 375 and 800nm.

It may be observed from Figure 3.4 that all Ag nanoparticle samples exhibit an asymmetric LSP peak except the sample with pto-ATP added at the synthesis, which has no LSP peak around 400nm. As appears from Table 3.1, the addition of ATP or pto-ATP to the Ag nanoparticles causes no significant shift of λ_{max}. However, the absorbance at λ_{max} decreases when ATP is added during particle synthesis and pto-ATP is added after the synthesis. Addition of ATP after nanoparticle synthesis does not influence the absorbance at λ_{max} though a small shoulder appears in the absorbance spectrum at ~450nm. The FWHM increases by the addition of both ATP and pto-ATP, though the addition of ATP after Ag nanoparticle synthesis causes only a 10nm increase whereas addition of ATP during synthesis causes a ~20nm increase. The addition of pto-ATP after the Ag nanoparticle synthesis entails a 60nm increase of the FWHM, which is the largest observed increase.

The development in time of the absorbance spectrum of unstabilized Ag nanoparticles is depicted in Figure 3.5 and Table 3.1. It is evident that λ_{max} of the LSP peak is slightly red-shifted and that the FWHM is reduced with time. The red-shift is about 5nm in 44 days,

whereas the reduction in FWHM is about 30nm. Furthermore, the peak becomes more symmetric with time and the absorbance at the λ_{max} increases by 12%.

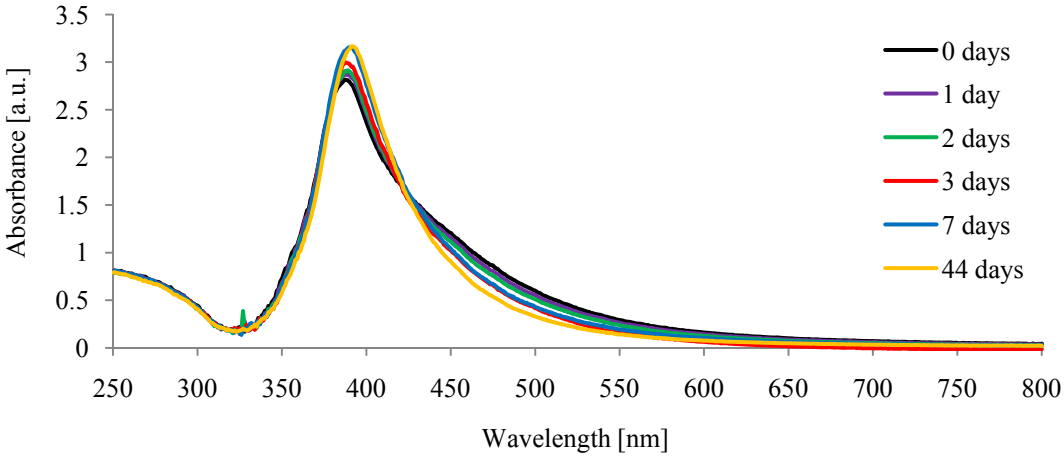

Figure 3.5: Absorbance spectra of unstabilized Ag nanoparticles recorded at the day of synthesis and after 1, 2, 3, 7, and 44 days. The x- and y-axis represent absorbance wavelength in nm and absorbance, respectively.

A similar, but more pronounced effect is observed from Ag nanoparticles with ATP added during the synthesis, as appears from Figure 3.6 and Table 3.1. In this case, λ_{max} increases by 9nm and the FWHM decreases by 66nm. The intensity of the absorbance measured at λ_{max} increases by 24%. A similar effect was not clearly observed when ATP was added to the Ag nanoparticles after the synthesis. In this case λ_{max} remains unchanged, whereas the FWHM decreases by 5nm and the intensity at λ_{max} decreases to 90% of the initial value after 44 days.

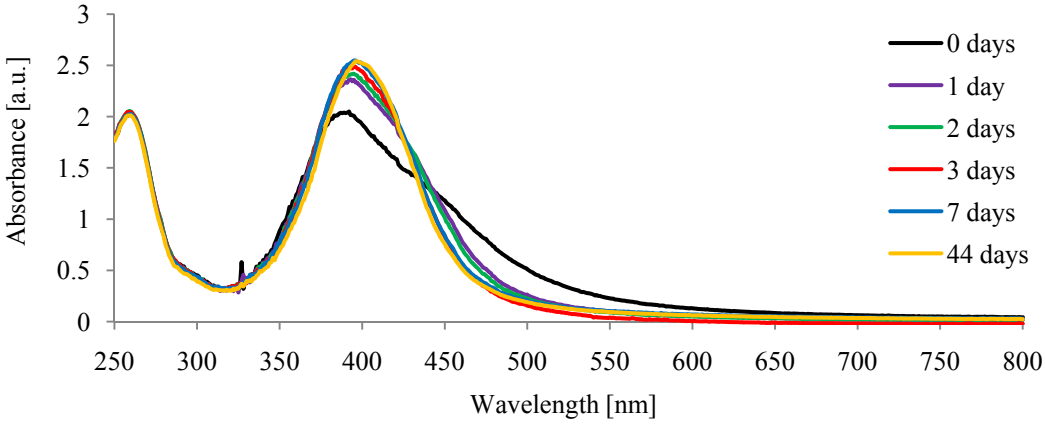

Figure 3.6: Absorbance spectra of Ag nanoparticles with ATP during particle synthesis. The spectra were recorded at the day of synthesis, and after 1, 2, 3, 7, and 44 days. The x- and y-axis represent absorbance wavelength in nm and absorbance, respectively.

In contrary to the effect observed from unstabilized Ag nanoparticles and particles with ATP added during the synthesis, the intensity at λ_{max} of particles with pto-ATP added after the synthesis decreases significantly to 42% of the initial value after 44 days, as emerges from Table 3.1. In 44 days the FWHM increases by ~225nm, whereas λ_{max} increases by ~17nm. Furthermore, a small shoulder is present in all the spectra, as can be observed in

Figure 3.7. The shoulder is present at a wavelength of ~450nm immediately after the nanoparticle synthesis. However, 3 days after the synthesis it is red-shifted to ~480nm and after 44 days it is present at ~550nm. The absorbance spectra of Ag nanoparticles with pto-ATP added during synthesis do not change in time (data not shown).

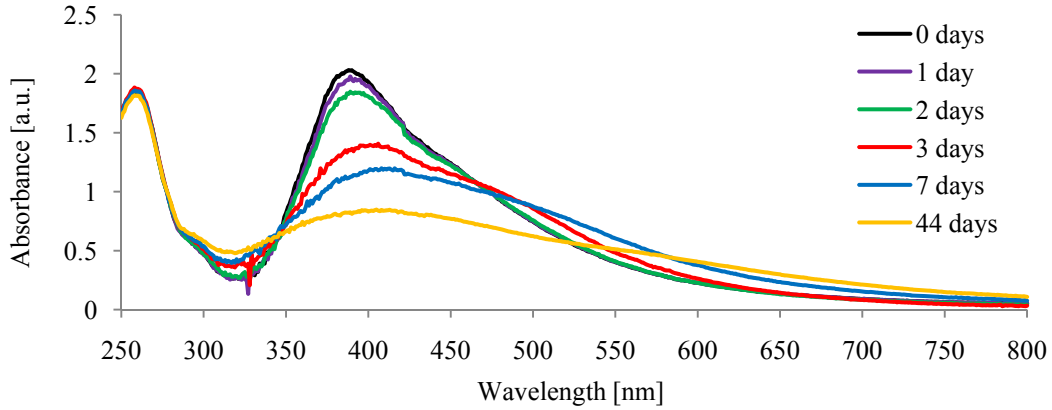

Figure 3.7: Absorbance spectra of Ag nanoparticles with pto-ATP added after the particle synthesis. The spectra were recorded at the day of synthesis, and after 1, 2, 3, 7, and 44 days. The x- and y-axis represent absorbance wavelength in nm and absorbance, respectively.

3.2.2 Effect of NaCl on ATP or pto-ATP Stabilized Ag Nanoparticles

The effect of adding NaCl to unmodified Ag nanoparticles and to ATP and pto-ATP stabilized particles can be observed from the absorbance spectra in Figure 3.8 and the λ_{max} and FWHM in Table 3.2 . The spectra have been produced by normalization of each spectrum at λ_{max}.

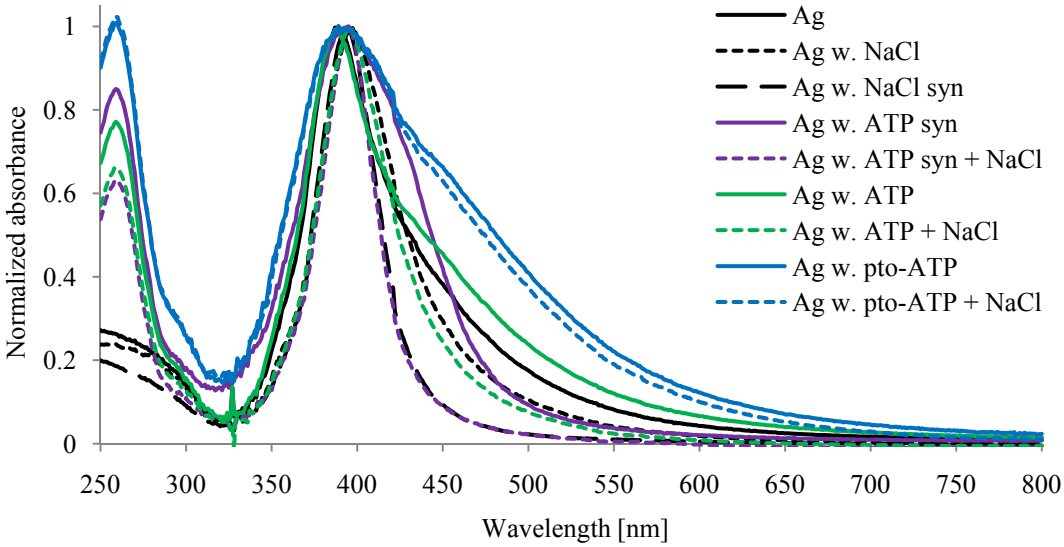

Figure 3.8: Normalized absorbance spectra of Ag nanoparticles without (Ag) and with NaCl added during (Ag w. NaCl syn) or after the synthesis (Ag w. NaCl). Furthermore, spectra of Ag nanoparticles with ATP added at the synthesis without (Ag w. ATP syn) and with NaCl (Ag w. ATP syn + NaCl) are depicted, along with spectra with ATP added after the synthesis without (Ag w. ATP) and with NaCl (Ag w. ATP + NaCl). Finally, absorbance spectra of Ag nanoparticles with pto-ATP added after the synthesis without (Ag w. pto-ATP) and with NaCl (Ag w. pto-ATP + NaCl) are shown. In the samples containing NaCl and ATP or pto-ATP the NaCl was added after the synthesis. All spectra were normalized at λ_{max}, and the x- and y-axis represent absorbance wavelength in nm and normalized absorbance, respectively.

Addition of 20mM NaCl to bare Ag nanoparticles causes a ~10nm red-shift of λ_{max} and a ~33nm decrease of the FWHM when the NaCl is added after the synthesis. However, when NaCl is added during the synthesis λ_{max} is red-shifted by ~5nm and the FWHM decreases by ~48nm. In comparison, addition of NaCl to nanoparticles with ATP added during the synthesis does not shift λ_{max}, whereas the FWHM of the plasmon peak is decreased by approximately 52nm to only ~38nm. NaCl addition also affects Ag nanoparticles with ATP added after the synthesis. In this case λ_{max} is red-shifted by ~8nm and the FWHM is decreased by ~65nm. It may be remarked that the spectrum of Ag nanoparticles with NaCl and ATP added after the synthesis resembles the spectrum of bare Ag nanoparticles in the presence of NaCl. Finally, addition of NaCl to Ag nanoparticles with pto-ATP added after the synthesis does not affect the absorbance spectrum significantly, as no shift of λ_{max} is observed and the FWHM is decreased by only ~12nm. In summary, addition of NaCl causes the LSP peaks in all spectra to narrow, and, except for the particles with pto-ATP, the peaks become more symmetric, as the fitting of the Lorentzian curve is more accurate.

Sample	λ_{max} [nm]	FWHM [nm]	R^2
Ag	389	99.1±0.9	0.99185
Ag w. NaCl	398.8±0.1	65.5±0.4	0.99719
Ag w. NaCl syn	393.6±0.1	40.9±0.2	0.99829
Ag w. ATP syn	395	89.9±0.8	0.99304
Ag w. ATP syn + NaCl	394.5±0.0	38.2±0.1	0.99935
Ag w. ATP	389	124.2±1.5	0.98631
Ag w. ATP + NaCl	397.0±0.1	59.5±0.3	0.99792
Ag w. pto-ATP	389	193.4±1.1	0.99723
Ag w. pto-ATP + NaCl	389	181.3±1.0	0.99720

Table 3.2: Wavelength of maximum absorbance (λ_{max}) and full width at half maximum (FWHM) of the LSP band deduced from the absorbance spectra in Figure 3.8. When no uncertainty is stated λ_{max} is read from the absorbance spectra, whereas FWHM and λ_{max} stated with uncertainties were obtained by fitting a Lorentzian curve to the absorption peak from the data between 375 and 800nm.

3.2.3 Binding of hp-DNA to ATP or pto-ATP Stabilized Ag Nanoparticles

Binding of DNA to the ATP or pto-ATP stabilized Ag nanoparticles is necessary for further use of the nanoparticles for binding to an Au surface. Therefore, the effect of hp-DNA binding on the stability of the particles was examined. In Figure 3.9 the absorbance spectra of the Ag nanoparticles with and without added hp-DNA can be observed, whereas λ_{max} and FWHM of the LSP peaks are depicted in Table 3.3.

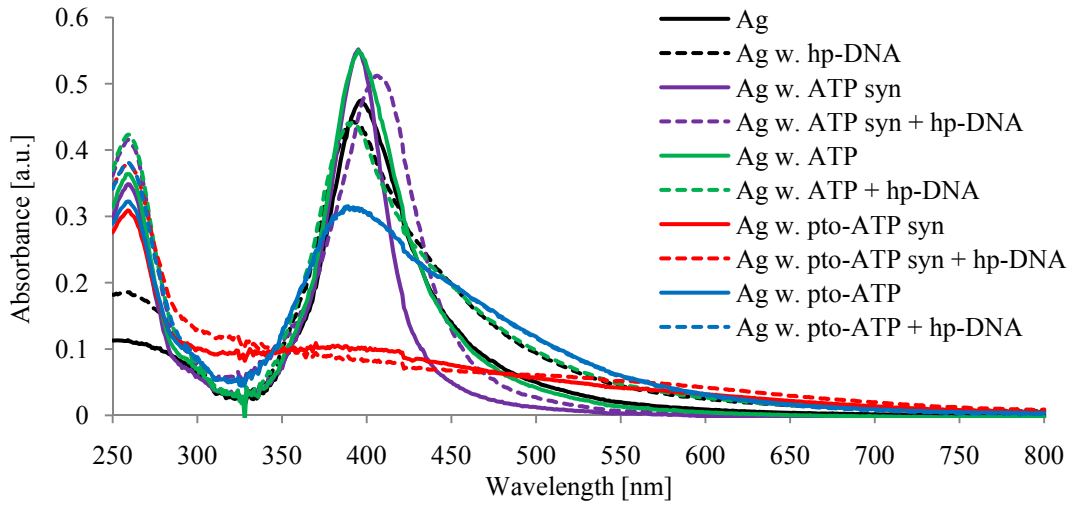

Figure 3.9: Absorbance spectra of bare Ag nanoparticles (Ag) and nanoparticles with hp-DNA present (Ag w. Hp-DNA). Furthermore, spectra of particles with ATP added during the synthesis in the absence (Ag w. ATP syn) and presence (Ag w. ATP syn + hp-DNA) of hp-DNA are shown along with spectra of particles with ATP added after the synthesis in the absence (Ag w. ATP) and presence (Ag w. ATP + hp-DNA) of hp-DNA. Finally, spectra of Ag nanoparticles with pto-ATP added during the synthesis with (Ag w. pto-ATP syn) and without (Ag w. pto-ATP syn + hp-DNA) hp-DNA present are depicted together with spectra of particles with pto-ATP added after the synthesis in the absence (Ag w. pto-ATP) and presence (Ag w. pto-ATP + hp-DNA) of hp-DNA. All spectra were measured with 20mM NaCl present in the samples. The x- and y-axis on the graph represent absorbance wavelength in nm and absorbance, respectively.

The presence of hp-DNA causes the FWHM to increase by 47, 17, and 53nm of both bare Ag nanoparticles and particles with ATP added during or after the synthesis, respectively, and the spectra all become less symmetric. However, the presence of hp-DNA does not affect λ_{max} similarly in the three samples, as it is red-shifted by 11nm in the sample with ATP added during the synthesis and blue-shifted by 8 and 6nm in the samples with unmodified particles and with ATP added after the synthesis. The presence of hp-DNA causes the already very small and broad LSP peak of the absorbance spectrum of Ag nanoparticles with pto-ATP added during the synthesis to disappear completely. In contrary, the Ag nanoparticles with pto-ATP added after the synthesis are not affect at all. The intensity measured at λ_{max} is decreased by the addition of hp-DNA to the remaining samples.

Sample	λ_{max} [nm]	Intensity at λ_{max}	FWHM [nm]	R^2
Ag	398.8±0.1	0.469	65.5±0.4	0.99719
Ag w. hp-DNA	391.0±0.5	0.443	112.9±1.3	0.99414
Ag w. ATP syn	394.5±0.0	0.552	38.2±0.1	0.99935
Ag w. ATP syn + hp-DNA	405.5±0.1	0.512	54.6±0.2	0.99837
Ag w. ATP	397.0±0.1	0.546	59.5±0.3	0.99792
Ag w. ATP + hp-DNA	391	0.441	113.5±1.1	0.99219
Ag w. pto-ATP syn	380	0.105	294.6±2.8	0.99227
Ag w. pto-ATP syn + hp-DNA	-	-	-	-
Ag w. pto-ATP	389	0.315	181.3±1.0	0.99720
Ag w. pto-ATP + hp-DNA	389	0.312	181.3±0.9	0.99747

Table 3.3: Wavelength of maximum absorbance (λ_{max}) and full width at half maximum (FWHM) of the LSP band deduced from the spectra in Figure 3.9. When no uncertainty is stated λ_{max} is read from the absorbance spectra, whereas FWHM and λ_{max} stated with uncertainties were obtained by fitting a Lorentzian curve to the absorption peak from the data between 375 and 800nm.

3.2.4 Stabilization of Ag Nanoparticles with DNA

Apart from attempting stabilization of Ag nanoparticles with ATP or pto-ATP it was also tried to stabilize the nanoparticles with short DNA strands. The absorbance spectra of Ag nanoparticles with DNA of four different sequences present at concentrations of 1.43μM and 2.86μM may be observed in Figure 3.10. The λ_{max} and FWHM calculated from the spectra are depicted in Table 3.4.

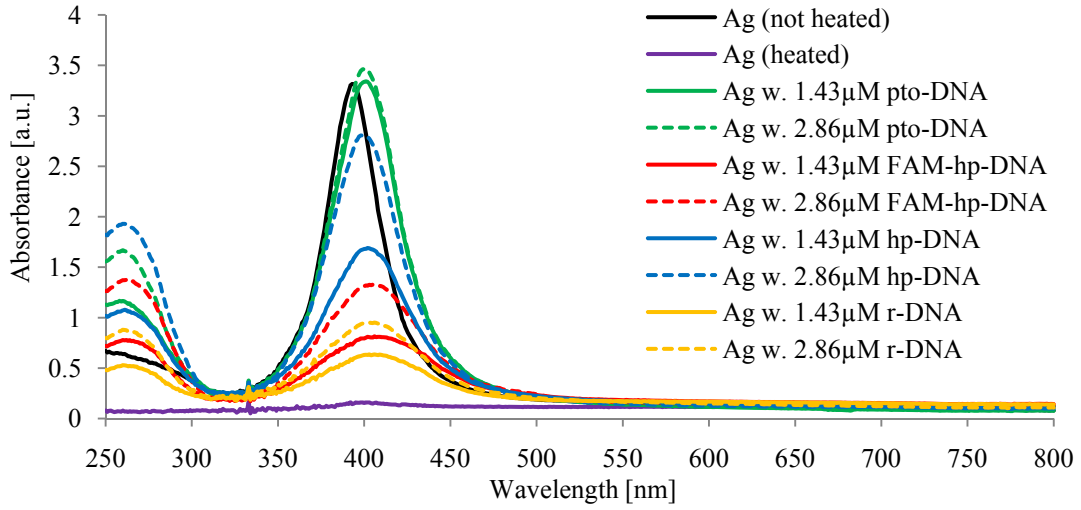

Figure 3.10: Absorbance spectra of Ag nanoparticles that were heated to 60°C for 2h (Ag (heated)) and unheated particles (Ag (not heated)) are depicted. Additionally, spectra of Ag nanoparticles with 1.43µM pto-DNA (Ag w. 1.43µM pto-DNA), FAM-hp-DNA (Ag w. 1.43µM FAM-hp-DNA), hp-DNA (Ag w. 1.43µM hp-DNA), or r-DNA (Ag w. 1.43µM r-DNA) present are shown along with spectra of particles with 2.86µM pto-DNA (Ag w. 2.86µM pto-DNA), FAM-hp-DNA (Ag w. 2.86µM FAM-hp-DNA), hp-DNA (Ag w. 2.86µM hp-DNA), or r-DNA (Ag w. 2.86µM r-DNA) present. All samples containing DNA were heated to 60°C for 2h. The graph is made with the x- and y-axis representing absorbance wavelength in nm and absorbance, respectively.

From the absorbance spectra it appears that heating of Ag nanoparticles causes the LSP peak to disappear almost completely. It was succeeded to fit a Lorentzian curve to the spectrum of the heated particles, though the fit was inaccurate. Compared to the unheated nanoparticles, stabilization of Ag nanoparticles with DNA of the four sequences all resulted in red-shift of λ_{max} and increase of the FWHM. The presence of pto-DNA at concentrations of 1.43µM and 2.86µM entailed a λ_{max} red-shift of 7nm at both concentrations and an increase in the FWHM values of 9 and 8nm, respectively, when compared to unheated particles. This is the lowest increase in FWHM observed among the four DNA sequences, and furthermore the absorbance measured at λ_{max} is highest in the two samples containing pto-DNA with the intensity being marginally higher in the sample with the higher DNA concentration. The fact that the intensity at λ_{max} is higher at the higher DNA concentration applies to the samples with either of all four DNA sequences.

Stabilization of Ag nanoparticles with FAM-hp-DNA causes the largest red-shifts of λ_{max} compared to bare nanoparticles that were not heated. The red-shifts are 14 and 11nm at DNA concentrations of 1.43 and 2.86µM, whereas the FWHM values are increased by 41 and 29nm, respectively. In comparison, the LSP peak of Ag nanoparticles stabilized with hp-DNA, which differs from FAM-hp-DNA by the presence of a thiol linker at the 5' end and the absence of the FAM fluorophore, is red-shifted by 9 and 6nm at hp-DNA concentrations of 1.43 and 2.86µM, respectively. This is a 5nm smaller red-shift at both concentrations than that entailed by FAM-hp-DNA. The FWHM increases caused at the low and high hp-DNA concentrations are 21 and 12nm, respectively, which is also smaller than the increases caused by FAM-hp-DNA. It can furthermore be observed from the absorbance spectra of FAM-hp- and hp-DNA stabilized Ag nanoparticles that the absorbance at λ_{max} is higher when hp-DNA is present, even when comparing the high concentration of FAM-hp-DNA and the low concentration of hp-DNA.

Finally, it emerges that compared to unheated Ag nanoparticles r-DNA causes red-shifts of λ_{max} of 12 and 10nm at the DNA concentrations of 1.43 and 2.86µM, respectively, and that the FWHM is increased by 32nm at both concentrations. The absorbance at λ_{max} of Ag nanoparticles stabilized with 2.86µM r-DNA is higher than the absorbance at λ_{max} of Ag nanoparticles stabilized with 1.43µM FAM-hp-DNA. Though, it is lower than when 2.86µM FAM-hp-DNA is present. The Ag nanoparticles stabilized with 1.43µM r-DNA yields the lowest absorbance at λ_{max} of all the samples containing DNA.

Sample		**λ_{max} [nm]**	**FWHM [nm]**	**R^2**
Ag (not heated)		393.3±0.0	36.3±0.1	0.99924
-||-	5 days	393.2±0.0	28.4±0.1	0.99844
-||-	7 days	394.0±0.0	31.2±0.1	0.99902
-||-	15 days	395.0±0.2	41.0±0.7	0.97592
-||-	22 days	397.2±0.2	37.0±0.6	0.97836
Ag (heated)		403.0±0.3	32.0±1.1	0.90637
-||-	5 days	402.5±0.5	35.5±1.7	0.82942
-||-	7 days	404.6±0.6	26.1±1.9	0.64912
-||-	15 days	404.1±0.4	64.3±1.3	0.96877
-||-	22 days	407.0±0.5	54.9±1.8	0.91711
Ag w. 1.43µM pto-DNA		400.7±0.0	45.9±0.2	0.99913
-||-	5 days	400.9±0.0	45.5±0.2	0.99890
-||-	7 days	400.8±0.1	44.8±0.2	0.99829
-||-	15 days	400.8±0.0	45.7±0.1	0.99917
-||-	22 days	400.9±0.0	45.4±0.2	0.99910
Ag w. 1.43µM FAM-hp-DNA		407.2±0.1	77.6±0.4	0.99781
-||-	5 days	404.0±0.1	65.0±0.5	0.99633
-||-	7 days	402.7±0.1	62.9±0.3	0.99794
-||-	15 days	401.2±0.1	60.9±0.3	0.99867
-||-	22 days	401.4±0.1	57.7±0.3	0.99854
Ag w. 1.43µM hp-DNA		401.9±0.1	57.5±0.2	0.99885
-||-	5 days	400.7±0.1	53.1±0.2	0.99907
-||-	7 days	400.1±0.1	52.0±0.2	0.99904
-||-	15 days	399.6±0.1	51.2±0.2	0.99847
-||-	22 days	399.6±0.1	50.0±0.2	0.99893
Ag w. 1.43µM r-DNA		405.8±0.1	68.3±0.5	0.99604
-||-	5 days	404.2±0.2	59.2±0.5	0.99368
-||-	7 days	402.6±0.2	55.3±0.5	0.99262
-||-	15 days	400.7±0.1	54.8±0.3	0.99723
-||-	22 days	400.6±0.1	51.3±0.4	0.99612
Ag w. 2.86µM pto-DNA		400.6±0.1	44.9±0.2	0.99859
-||-	5 days	401.0±0.1	45.6±0.2	0.99882
-||-	7 days	401.0±0.1	45.5±0.2	0.99891
-||-	15 days	401.2±0.0	46.3±0.1	0.99924
-||-	22 days	401.3±0.0	46.2±0.2	0.99913

Ag w. 2.86µM FAM-hp-DNA		404.2±0.1	65.8±0.3	0.99838
-||-	5 days	401.9±0.1	58.5±0.3	0.99739
-||-	7 days	401.1±0.1	57.0±0.3	0.99851
-||-	15 days	400.1±0.1	56.2±0.2	0.99918
-||-	22 days	400.3±0.1	54.3±0.2	0.99883
Ag w. 2.86µM hp-DNA		399.7±0.1	48.7±0.2	0.99845
-||-	5 days	399.5±0.1	48.5±0.2	0.99863
-||-	7 days	399.3±0.1	47.9±0.2	0.99879
-||-	15 days	399.0±0.0	48.5±0.1	0.99933
-||-	22 days	399.2±0.0	48.0±0.2	0.99917
Ag w. 2.86µM r-DNA		403.9±0.1	68.7±0.4	0.99800
-||-	5 days	402.3±0.1	64.2±0.3	0.99804
-||-	7 days	401.1±0.1	57.2±0.2	0.99888
-||-	15 days	399.6±0.1	56.2±0.3	0.99829
-||-	22 days	399.5±0.1	54.8±0.2	0.99883

Table 3.4: Wavelength of maximum absorbance (λ_{max}) and full width at half maximum (FWHM) of the LSP band deduced from the spectra in Figure 3.10, and from spectra of the samples measured after 5, 7, 15, and 22 days. When no uncertainty is stated λ_{max} is read from the absorbance spectra, whereas FWHM and λ_{max} stated with uncertainties were determined by fitting a Lorentzian curve to the absorption peak from the data between 375 and 800nm.

The development in time of the absorbance measured at λ_{max} of the Ag nanoparticles stabilized with DNA may be observed in Figure 3.11, whereas the development of λ_{max} and FWHM are depicted in Table 3.4.

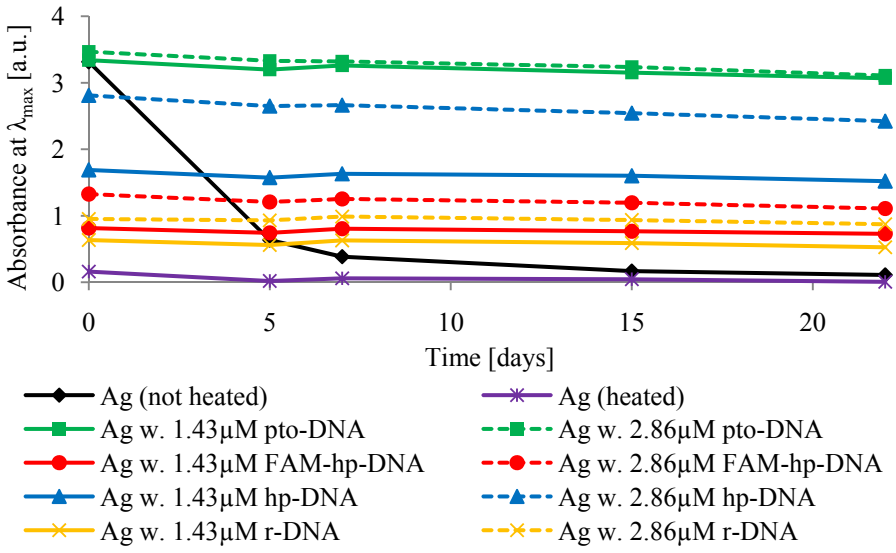

Figure 3.11: Absorbance measured at λ_{max} of the samples in Figure 3.10. The absorbance was measured after 0, 5, 7, 15, and 22 days. The x- and y-axis represent time in days and absorbance measured at λ_{max}, respectively.

As can be observed from Figure 3.11, the absorbance at λ_{max} of unheated Ag nanoparticles has decreased to ~12% of the initial value after 7 days, whereas the absorbance at λ_{max} of none of the DNA stabilized Ag nanoparticles decrease to a value less than 83% of the initial

value within 22 days. It emerges from Table 3.4 that λ_{max} of the unheated Ag nanoparticles increases by 4nm in 22 days, and furthermore, the fitting of the Lorentzian curve generally becomes more inaccurate with time. A 4nm increase in λ_{max} of the heated Ag nanoparticles is also observed in 22 days, though the fitting of the Lorentzian curve to the absorbance spectrum is very inaccurate. In contrary, the λ_{max} and FWHM values of Ag nanoparticles stabilized with 1.43 or 2.86µM pto-DNA or 2.86µM hp-DNA remain stable, as all of them shift by less than 1nm. The λ_{max} and FWHM of the particles stabilized with 1.43µM decrease by 2 and 7nm, respectively. For comparison, the λ_{max} and FWHM for Ag nanoparticles with 1.43µM FAM-hp-DNA decrease by 6 and 20nm, which are the largest decreases observed, and by 4 and 11nm for particles with 2.86µM FAM-hp-DNA. Decreases are also observed for r-DNA stabilized particles. In this case λ_{max} and FWHM decrease by 5 and 17nm when 1.43µM DNA is present and 4 and 14nm with 2.86µM present.

3.3 Gel Electrophoresis of DNA or ATP Stabilized Ag Nanoparticles

The mobility of nanoparticles in an electrophoresis gel depends on the charge and size of the particles, as the mobility decreases with increasing size and increases with increasing charge. Furthermore, the mobility is influenced by molecules adsorbed at the particles surface, since adsorbed molecules may increase the effective size of the particles and change the overall charge. The mobility and stability of Ag nanoparticles stabilized with 2.86µM DNA or 28.6µM ATP was examined in an agarose gel, which is presented in Figure 3.12.

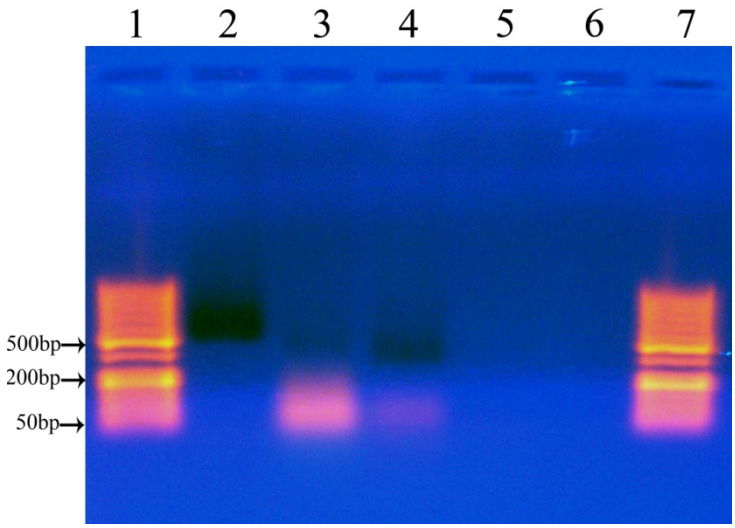

Figure 3.12: 1% agarose gel electrophoresis of Ag nanoparticles stabilized with 2.86µM DNA or 28.6µM ATP. The lanes contain Ag nanoparticles stabilized with pto-DNA (lane 2), FAM-hp-DNA (lane 3), hp-DNA (lane 4), r-DNA (lane 5), and ATP (lane 6). A 50bp GeneRuler™ (Fermentas, Helsingborg, Sweden) DNA ladder was used (lanes 1 and 7).

In the gel the Ag nanoparticles are visible as dark bands while the DNA stained with ethidium bromide is visible as bright bands. It is evident from the agarose gel experiment that r-DNA and ATP stabilized Ag nanoparticles aggregate before they enter the gel, and therefore they do not form a band in the gel. On the other hand, pto-, FAM-hp-, and hp-DNA stabilized particles form bands in the gel. The pto-DNA stabilized particles form the most

intense band and have the lowest mobility of the three, whereas hp-DNA stabilized particles have the highest mobility and form the second most intense band. Bands originating from excess DNA present in the samples containing FAM-hp- and hp-DNA may also be observed, while no bands are evident from the single stranded pto- and r-DNA.

3.4 Atomic Force Microscopy on Ag Nanoparticles Linked to Au Surface

AFM was used in order to determine the ability of hp-DNA stabilized Ag nanoparticles to bind to an Au surface, and the ability of pto-DNA stabilized Ag nanoparticles to bind to ssDNA linked to an Au surface. AFM images of the immobilized hp-DNA stabilized Ag nanoparticles can be observed in Figure 3.13.

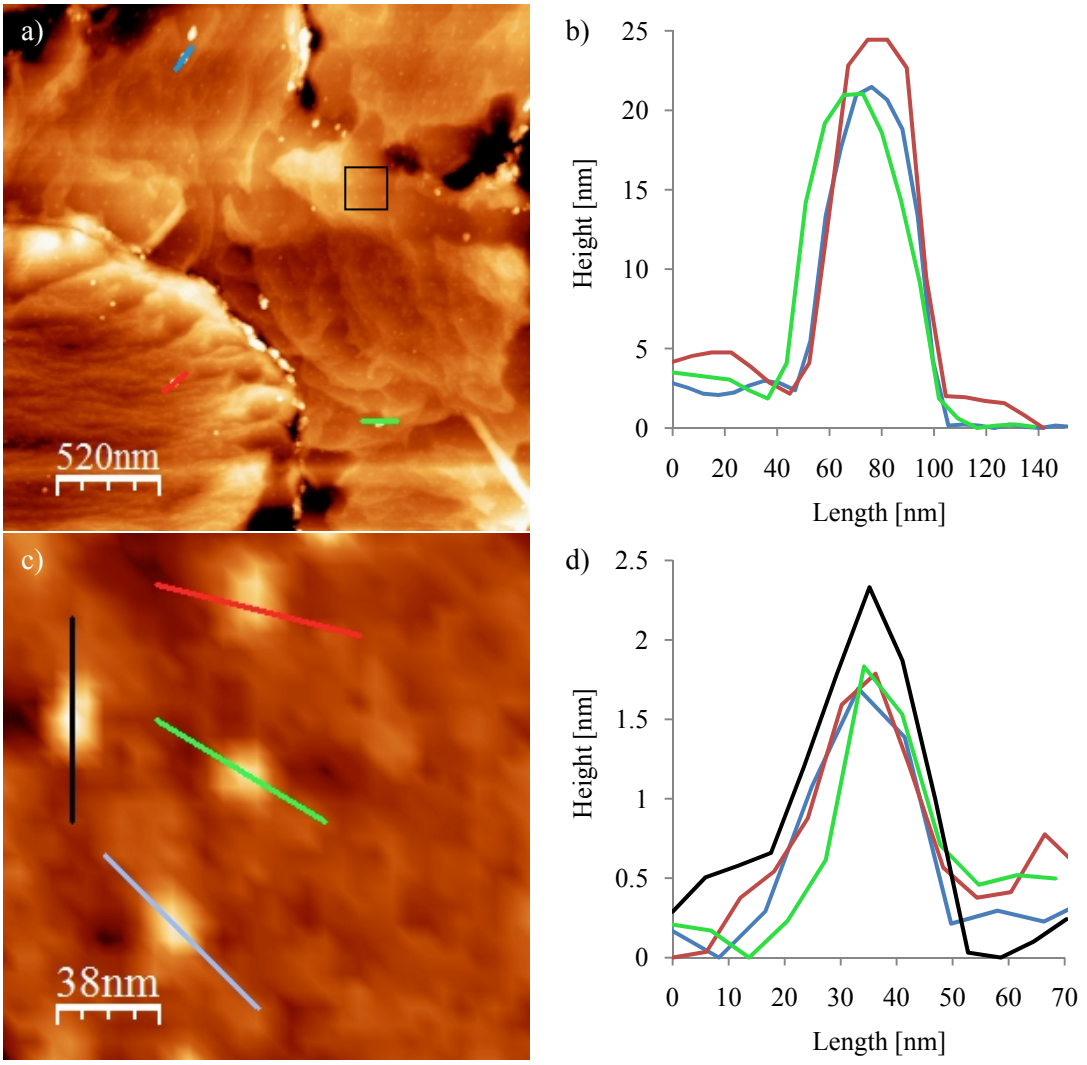

Figure 3.13: AFM image of hp-DNA stabilized Ag nanoparticles bound at a flame annealed Au surface (a). The coloured bars at the image mark height profiles of three Ag nanoparticles (b). Furthermore, a zoom represented by the box in (a) is shown (c), and height profiles marked by the coloured bars in the zoom are shown (d). The height profiles are presented in graphs with the x- and y-axis representing length and height, respectively, measured in nm.

The attempt to bind hp-DNA stabilized Ag nanoparticles on flame annealed gold is observed to result in binding of very few particles with sizes ranging from ~9nm to ~25nm, as may be observed in Figure 3.13a. Furthermore, it is observed that binding of hp-DNA to the surface occurs, as the height of B-form DNA in solution is 2.37nm and the height is expected to decrease at binding to the Au surface[58]. This is consistent with the heights measured in Figure 3.13d.

Images of pto-DNA stabilized Ag nanoparticles linked to flame annealed and SPR surfaces by hybridization of pto-DNA and thiol-DNA linked to the surface are depicted in Figure 3.14.

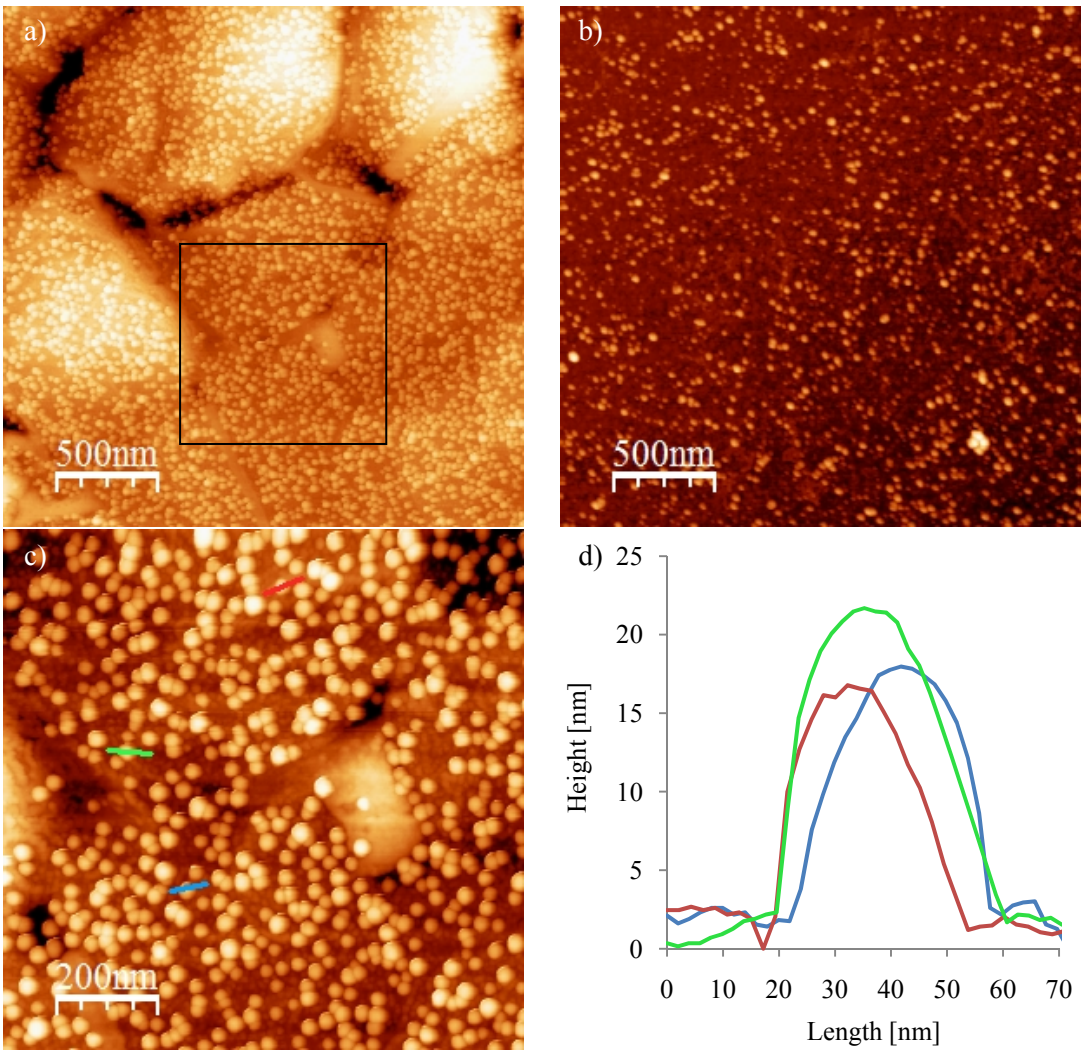

Figure 3.14: AFM images of pto-DNA stabilized Ag nanoparticles linked to flame annealed (a) and SPR (b) Au surface. Furthermore, a zoom represented by the box in (a) is shown (c), and height profiles marked by the coloured bars in the zoom are presented (d). The height profiles are presented in a graph with the x- and y-axis representing length and height, respectively, measured in nm.

The density of pto-DNA stabilized Ag nanoparticles at the flame annealed and SPR Au surfaces presented in Figure 3.14a and Figure 3.14b, respectively, are 569particles/μm^2 and 184particles/μm^2. That is, the binding of the nanoparticles is approximately three times more effective at the flame annealed Au surface. However, the densities of particles are higher on both surfaces compared to the flame annealed Au surface with bound hp-DNA stabilized

particles, which has a density of ~3.25particles/μm^2. The mean size of the pto-DNA stabilized particles obtained from the sizes of 30 arbitrarily chosen particles at the flame annealed and SPR Au surfaces are 16.5 and 15.3nm with standard deviations of 3.1 and 4.2nm, respectively.

3.5 Purification of IL-4

Chemically synthesized IL-4 used for binding to dsDNA was purified by FPLC on a size exclusion column. The chromatogram from the purification is shown in Figure 3.15.

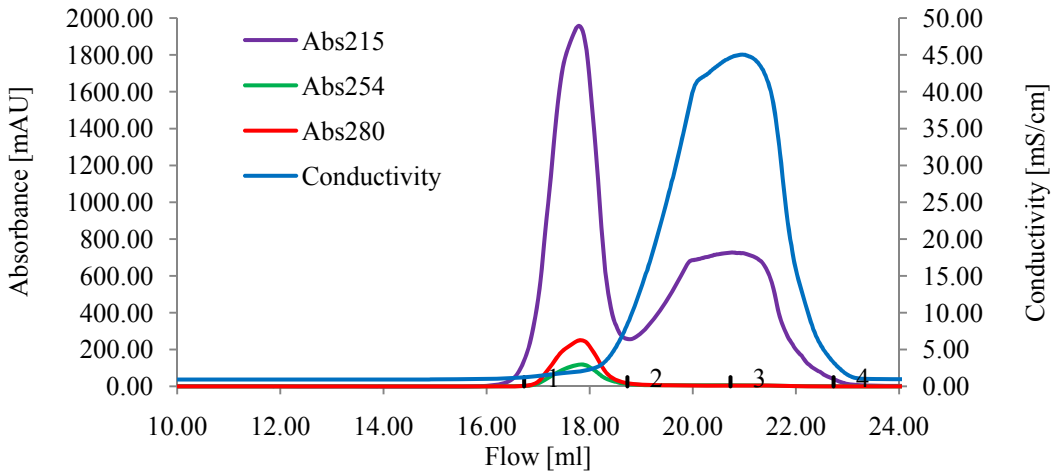

Figure 3.15: Chromatogram of IL-4 purification by FPLC. 500μl 1.5mg/ml IL-4 was loaded on the column and the eluted sample was fractionized into 2ml samples starting after 16.73ml, as marked on the x-axis. The pressure in the system was ~0.35MPa during the experiment. Absorbance was measured at 215nm (Abs215), 254nm (Abs254), and 280nm (Abs280) and furthermore the conductivity of the eluted sample was measured. The x-axis represents the volume flushed through the system measured in ml, whereas the y-axis to the left represents absorbance measured in milli-absorbance units and the y-axis to the right represents conductivity measured in mS/cm.

The tryptophan residue in IL-4 is expected to absorb light at the three wavelengths at which absorbance is measured, and it may therefore be used as an indicator of when IL-4 is eluted from the column[59]. As appears from the chromatogram, absorbance peaks of the three measured wavelengths at 215, 254, and 280nm are located at ~18ml, whereas an additional peak in the absorbance measured at 215nm is observed at ~21ml. The second peak of the absorbance measured at 215nm coincides with the only peak observed in the conductivity.

The sample from fraction 1 was freeze-dried and used for further SPR spectroscopy experiments.

3.6 IL-4 Binding Assay Based on Surface Plasmon Resonance

Binding of IL-4 to dsDNA without and with Ag nanoparticles was monitored in real-time by SPR spectroscopy in order to be able to determine the association and dissociation constants of the binding. Hereby it may be determined if the presence of Ag nanoparticles has an enhancing effect on the SPR shift observed at IL-4 binding or if it affects the reflectivity spectrum. Association rate constants (k_a), dissociation rate constants (k_d), and maximum

responses (Rmax) of the binding of IL-4 to dsDNA are obtained by fitting the binding curves to a 1:1 reaction model. An equilibrium binding constant (K_D) for the interaction may be calculated from the division of k_d by k_a[60].

A SPR sensorgram showing the binding of dsDNA to an Au surface and subsequent binding of IL-4 to the dsDNA can be observed in Figure 3.16. Additionally, binding curves of the binding between IL-4 and dsDNA are depicted along with k_a, k_d, Rmax, K_D, and standard deviation of the residuals of fits made to the curves (Res sd).

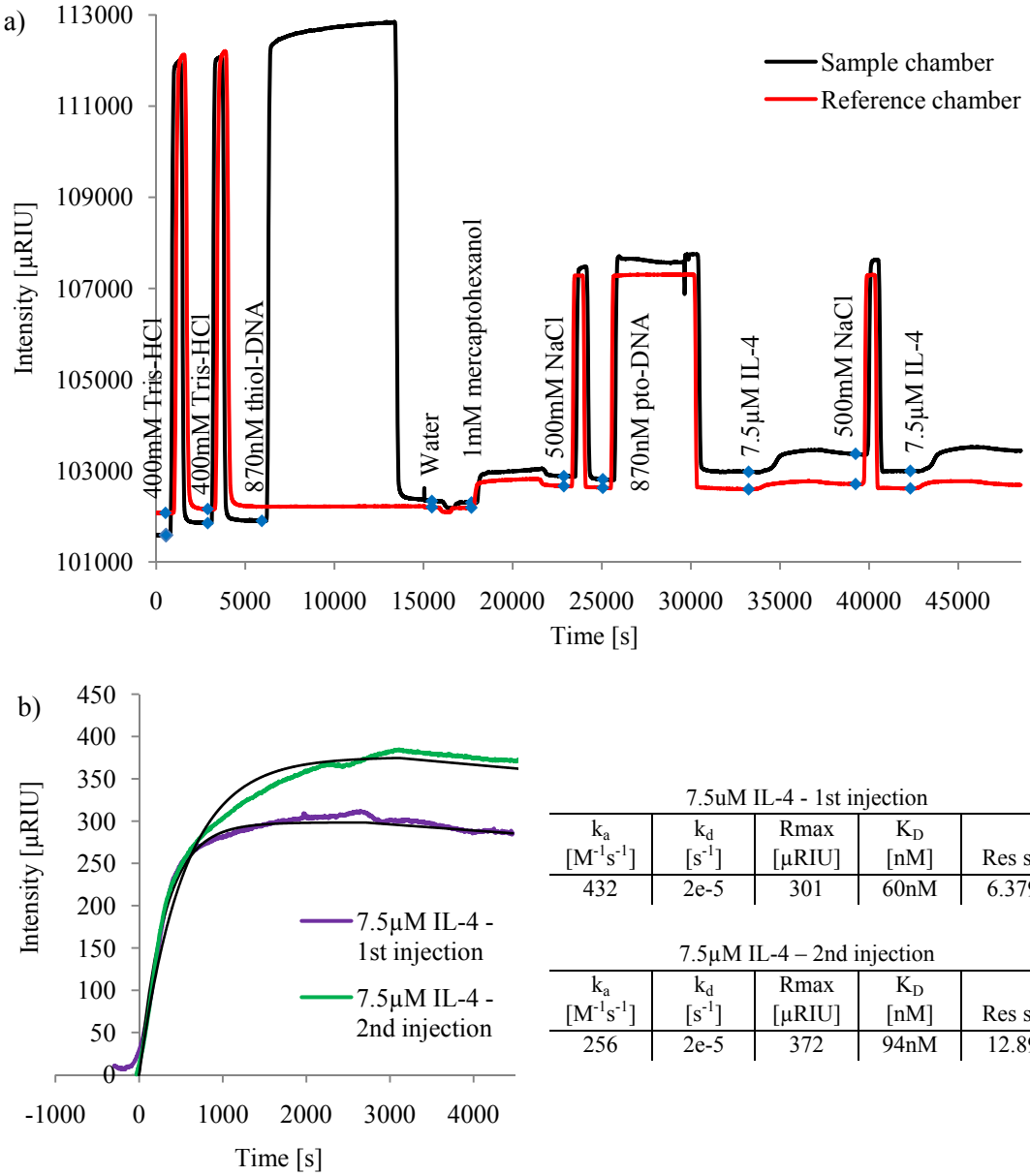

7.5uM IL-4 - 1st injection

k_a [$M^{-1}s^{-1}$]	k_d [s^{-1}]	Rmax [µRIU]	K_D [nM]	Res sd
432	2e-5	301	60nM	6.379

7.5µM IL-4 – 2nd injection

k_a [$M^{-1}s^{-1}$]	k_d [s^{-1}]	Rmax [µRIU]	K_D [nM]	Res sd
256	2e-5	372	94nM	12.89

Figure 3.16: SPR sensorgram of binding of dsDNA to Au surface without Ag nanoparticles present, and of IL-4 binding to the dsDNA (a). The beginning of the made injections are marked with blue dots and the substance is injected is stated next to the marks. Furthermore, binding curves of the two 7.5µM IL-4 injections are presented (b). The curves were made by subtracting the reference chamber signal from the sample chamber signal. The x- and y-axes in the two figures represent time in s and intensity measured in µRIU. The association and dissociation rate constants, the maximum response, the equilibrium binding constant, and the residual standard deviation of the fits are depicted in the tables.

Binding of dsDNA at the Au surface of the SPR sensor chip was done by initially linking thiol-DNA to the surface. In order to screen the negative charges of the DNA and thereby improve the surface coverage the DNA was suspended in a buffer with high ionic strength[61]. The injection of 870nM thiol-DNA, which was done in the sample chamber only, entails an increase of 454μRIU. The difference has been measured as the difference in signal immediately before the system was rewired the first time and after flow was established through both chambers again. The signal in the reference chamber decreases by 11μRIU in this period.

After thiol-DNA is bound to the surface, mercaptohexanol is injected in both chambers to block the surface in order to avoid unspecific binding of pto-DNA and IL-4, and furthermore to elute unspecifically bound thiol-DNA from the sample chamber[61]. The injection of mercaptohexanol causes increases of 570 and 468μRIU in the sample and reference chambers, respectively, when comparing before and after the injection. This step is followed by injection of pto-DNA, which has a sequence complementary to the sequence of thiol-DNA. The pto-DNA is injected in a suspension of 500mM NaCl in order to screen the charges on the DNA strands and thereby improve the hybridization of the two complementary DNA strands. As can be observed from Figure 3.16a, the injection of pto-DNA entails an increase of 190μRIU in the signal from the sample chamber, whereas the signal from the reference chamber remains unchanged. The dsDNA, which is expected to be formed on the Au surface, is used for subsequent monitoring of the binding of IL-4 to the DNA.

Binding curves of two injections of 7.5μM IL-4 are shown in Figure 3.16b. The curves were made by subtracting the signal from the reference chamber from the sample chamber signal. The fits to the binding curves of the IL-4 injections yield association rate constants of 432 and $256 M^{-1}s^{-1}$ for the first and second injection, respectively, whereas dissociation rate constants of $0.00002 s^{-1}$ were obtained from both curves. This results in equilibrium binding constants of 60nM for the first injection of 7.5μM IL-4 and 94nM for second injection. Between the two injections the surface is regenerated with 500mM NaCl, which entails a decrease of the signal from both chambers to a level 20μRIU higher than before the first IL-4 injection.

Reflectivity scans from the sample chamber measured before and after the injection of pto-DNA and after the 2^{nd} injection of 7.5μM IL-4 are depicted in Figure 3.17. As may be observed the binding of neither pto-DNA nor IL-4 causes significant changes to the width or the reflectivity at the minimum of the surface plasmon reflectivity dip.

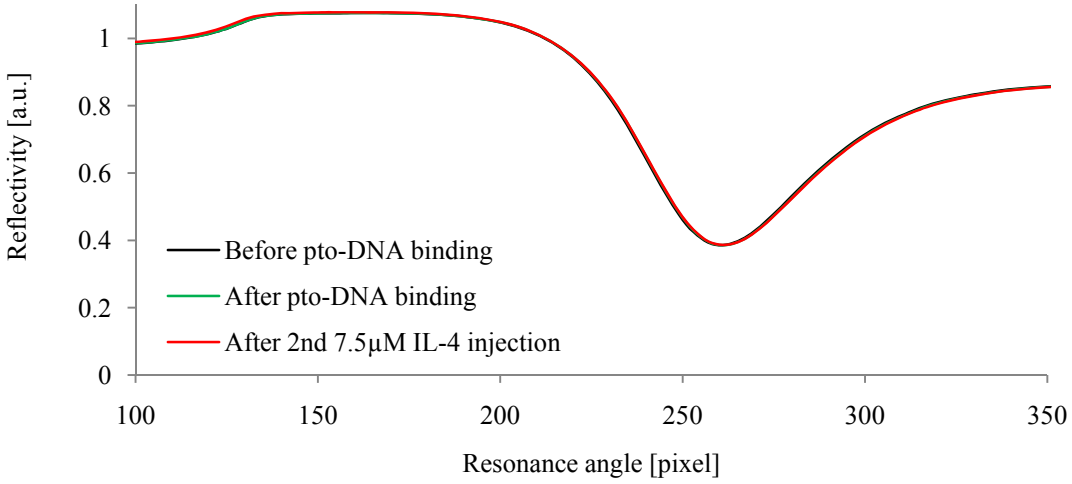

Figure 3.17: Sample chamber reflectivity scans measured before injection of pto-DNA (Before pto-DNA binding), after the injection of pto-DNA (After pto-DNA binding), and after the 2nd 7.5µM IL-4 injection (After 2nd 7.5µM IL-4 injection) in the experiment presented in Figure 3.16. The x- and y-axis represent resonance angle measured in pixels and reflectivity measured in arbitrary units.

In an experiment equivalent to the one presented in Figure 3.16, binding of IL-4 at concentrations of 0.1, 0.5, 2.5, and 7.5µM was attempted. However, a proper binding curve was only obtained from the first injection containing 0.1µM IL-4 (remaining data not shown). The curve and the fitted k_a, k_d, Rmax, K_D, and standard deviation of the residuals obtained by fitting are depicted in Figure 3.18.

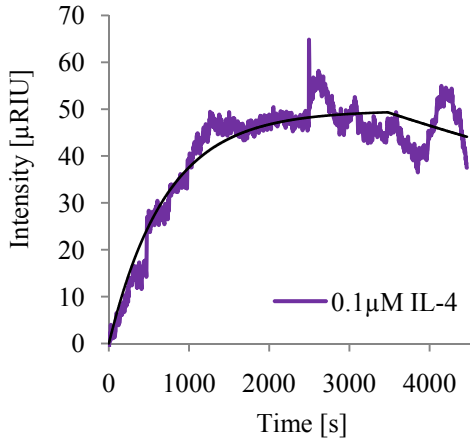

0.1µM IL-4				
k_a [$M^{-1}s^{-1}$]	k_d [s^{-1}]	Rmax [µRIU]	K_D [nM]	Res sd
1.30e4	1.1e-4	54	9nM	3.891

Figure 3.18: Binding curve of 0.1µM IL-4 injection made on dsDNA modified Au surface similar to the one shown in Figure 3.16. The curve was made by subtracting the reference chamber signal from the sample chamber signal. The x- and y-axis in the figure represent time in s and intensity measured in µRIU. The association and dissociation rate constants, the maximum response, the equilibrium binding constant, and the residual standard deviation of the fit are depicted in the table.

As appears from the figure, an association rate constant of $13000M^{-1}s^{-1}$ is obtained, which is two orders of magnitude larger than the association constants determined from the 7.5µM injections. Comparison of the dissociation rate constants reveals that the dissociation constant of $0.00011s^{-1}$ obtained from the 0.1µM injection is an order of magnitude larger than those obtained from the 7.5µM injections. The obtained equilibrium binding constant of

9nM are 7 and 10 times lower than those obtained from the first and second injections of 7.5µM IL-4, respectively.

The effect on IL-4 binding of Ag nanoparticles linked to the dsDNA was determined in an experiment similar to the one presented in Figure 3.16. The experiments differ by the fact that pto-DNA stabilized Ag nanoparticles were injected instead of pto-DNA in this experiment. The sensorgram of the experiment and binding curves of 7.5µM IL-4 can be observed in Figure 3.19.

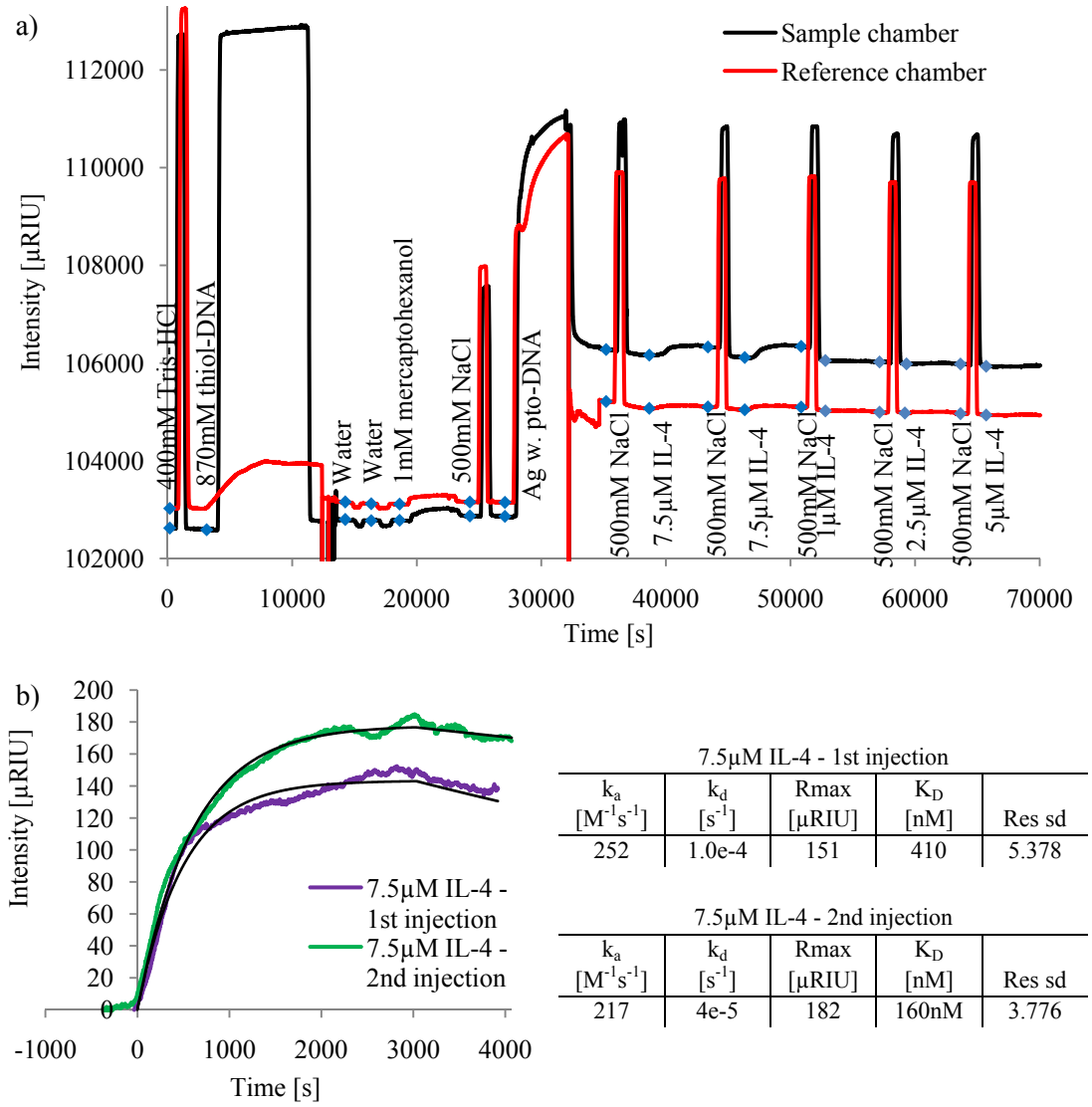

7.5µM IL-4 - 1st injection

k_a [$M^{-1}s^{-1}$]	k_d [s^{-1}]	Rmax [µRIU]	K_D [nM]	Res sd
252	1.0e-4	151	410	5.378

7.5µM IL-4 - 2nd injection

k_a [$M^{-1}s^{-1}$]	k_d [s^{-1}]	Rmax [µRIU]	K_D [nM]	Res sd
217	4e-5	182	160nM	3.776

Figure 3.19: SPR sensorgram of binding of dsDNA to Au surface with Ag nanoparticles present, and of IL-4 binding to the dsDNA interlinking the Au surface and the Ag nanoparticles (a). The beginning of the made injections are marked with blue dots, and the substance injected is stated next to the marks. Furthermore, binding curves of the two 7.5µM IL-4 injections are presented (b). The curves were made by subtracting the reference chamber signal from the sample chamber signal. The x- and y-axes in the two figures represent time in s and intensity measured in µRIU. The association and dissociation constants, the maximum response, the equilibrium binding constant, and the residual standard deviation of the fits are depicted in the tables.

The injection of thiol-DNA into the sample chamber is observed to result in an increase of the signal of 186µRIU. However, the reference chamber signal increases by 127µM whereas only a minor increase was observed in the experiment presented above. Binding of mercaptohexanol in the sample and reference chambers entails increases of 92 and 48µRIU, respectively. These increases only make up 16 and 10% of the increases observed in the SPR experiment presented above. However, the binding of pto-stabilized Ag nanoparticles entails increases of 3420 and 2055µRIU in the signals from the sample and reference chambers, respectively. The signal increase caused by binding of pto-DNA constitutes 6% of the increase observed in the sample chamber when pto-DNA stabilized Ag nanoparticles are bound.

Binding of IL-4 to the dsDNA interlinking Au surface and Ag nanoparticles resulted in the binding curves observed in Figure 3.19b. It was only possible to obtain binding curves from the two first injections with 7.5µM IL-4, whereas no signal increase was observed at the subsequent IL-4 injections with concentrations of 1.0, 2.5, and 5.0µM. The association rate constants of the first and second 7.5µM IL-4 injections are 252 and 217$M^{-1}s^{-1}$, respectively, whereas the dissociation rate constants are 0.00010 and 0.00005s^{-1}, and this yields equilibrium binding constants of 410 and 160nM. The presence of Ag nanoparticles results in equilibrium binding constants which are significantly higher than when no Ag nanoparticles are present, and the binding capacity of the surface is reduced, which is demonstrated by the lower Rmax.

Regeneration of the surface with 500mM NaCl after the first 7.5µM IL-4 injection entailed decreases by 50 and 21µRIU in the sample and reference chambers, respectively, compared to before the IL-4 injection, whereas decreases of 59 and 29µRIU were observed for the regeneration after the second 7.5µM IL-4 injection.

Reflectivity scans measured form the sample chamber before and after the injection of pto-DNA conjugated Ag nanoparticles and after the 2nd injection of 7.5µM IL-4 may be observed in Figure 3.20. The binding of pto-DNA modified Ag nanoparticles appears to cause an increase of the reflectivity at the minimum of the surface plasmon reflectivity dip while the width of the dip is not observed. The binding of IL-4 does not appear to change the width or the reflectivity at the minimum of the dip.

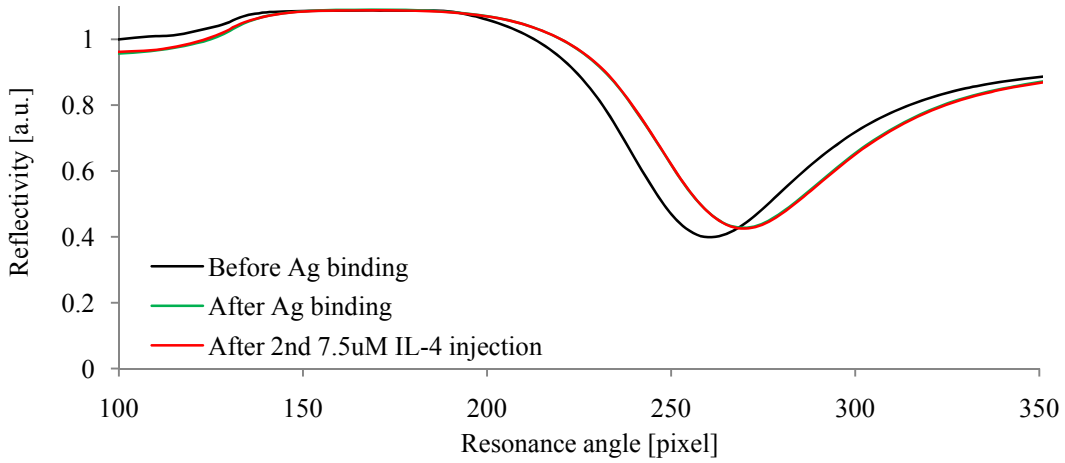

Figure 3.20: Sample chamber reflectivity scans measured before injection of pto-DNA modified Ag nanoparticles (Before Ag binding), after the injection of pto-DNA modified Ag nanoparticles (After Ag binding), and after the 2nd 7.5µM IL-4 injection (After 2nd 7.5µM IL-4 injection) in the experiment presented in Figure 3.19. The x- and y-axis represent resonance angle measured in pixels and reflectivity measured in arbitrary units.

4 Discussion

Ag nanoparticles are less used for the purpose of biosensing than Au nanoparticles despite the fact that Ag particles may be optically more interesting[12]. However, the Ag nanoparticles suffers from a lack of stability, which explains why they are less used[6]. Hence, in order to be able to use Ag nanoparticles for biosensing stabilization of the particles is necessary.

4.1 Stabilization of Ag Nanoparticles

The Ag nanoparticles used in this project were produced by adding the reducing agent $NaBH_4$ to a solution of $AgNO_3$. Hereby, the silver ions (Ag^+) are reduced by the borohydrides (BH_4^-) to form silver (Ag^0) and boron hydroxide ($B(OH)_3$), as depicted in the following equation[62]:

$$Ag^+ + BH_4^- + 3H_2O \rightarrow Ag^0 + B(OH)_3 + 3.5H_2 \qquad \textbf{Equation 4.1}$$

According to Nath and Chilkoti (2004) the particle formation proceeds in three steps[42]. In the first step a 1-2nm nanoparticle is formed by collisions between the reduced Ag^+ and in the second step the particle grows by reduction of Ag^+ on the surface of the particle. When reducing agent is in excess this step proceeds until all metal ions are reduced. Stabilization of the nanoparticle by adsorption of stabilizing agents occurs in the third step. Nanoparticles produced by use of BH_4^- as reducing agent are temporarily stabilized electrostatically by adsorption of BH_4^- and borate ions (BO_3^{3-}), which are formed by a side reaction between BH_4^- and water[9,62].

In the experiments described, the Ag nanoparticles were produced by mixing of 1mM $AgNO_3$ and 1mM $NaBH_4$ in a volume ratio of 1:3. Interestingly, the LSP peak observed immediately after synthesis is always asymmetric. This indicates that the synthesized nanoparticles are polydisperse or that the particles have aggregated after the synthesis, whereby aggregates of different sizes are present in the solution[21,63,64,65]. If the asymmetry is caused by polydispersity, it may be caused by a deficit of reducing and stabilizing agent. By increasing the amount of reducing agent, more nuclei are formed in the first step of the particle formation, whereby smaller and more monodisperse particles are formed[42]. Furthermore, when the BH_4^- concentration is too low the $B(OH)_3$ produced at the reduction of the Ag^+ may compete with BH_4^- and BO_3^{3-} for adsorption on the nanoparticles[62]. As $B(OH)_3$ is uncharged it does not provide electrostatic stabilization whereby particle aggregation may occur. An increase in the amount of stabilizing agent is also able to provide higher homogeneity of the nanoparticle solution as this slows down the growth of the nanoparticles due to the adsorption of more stabilizing molecules on the nanoparticles. Hereby, the diffusion of Ag^+ to the nanoparticle surfaces is slowed down whereby the growth becomes more uniform and the final result is a more monodisperse particle solution. If the asymmetry of the LSP peak is caused by aggregation after the particle synthesis, an increase in the amount of stabilizing agent provides larger repulsion between the particles and thereby the aggregation is reduced. It cannot be determined whether the asymmetry of

the Ag nanoparticle LSP peak is caused by polydispersity from the synthesis or by aggregation. In order to solve this issue, an additional technique needs to be applied, such as AFM or transmission electron microscopy (TEM) imaging. Still, both possibilities may explain why the Ag nanoparticles with NaCl added during nanoparticle synthesis appears monodisperse, as the chloride ions may function as stabilizing agent. The monodispersity is indicated by the almost perfectly symmetric LSP peak and with a 58% lower FWHM than the peak of the Ag nanoparticles without NaCl. The improved symmetry of the absorbance spectrum of particles with NaCl added after the synthesis indicates that NaCl also increases the monodispersity when added at this point. This indicates that the Ag nanoparticles without NaCl present are aggregated, at least to some extent, and that the aggregation is partly reversible at the addition of NaCl. However, the LSP peak of particles with NaCl added after the synthesis is less symmetric than when the salt is added during the synthesis and the nanoparticle solution is therefore not monodisperse. This may be due to a lower surface density of adsorbed chloride ions on the particles where NaCl is added after the synthesis. The presence of NaCl is also observed to slightly red-shift λ_{max} both when it is added during and after the synthesis. The red-shifts are relatively small and therefore they are probably caused by the fact that NaCl increases the permittivity in the vicinity of the nanoparticles. Particle aggregation may also be indicated by red-shifting of the LSP peak, though the expected red-shift is larger than what is observed in this case[66].

When considering the time development of the absorbance spectra of unmodified Ag nanoparticles and particles with NaCl added during or after the synthesis it emerges that the unmodified Ag nanoparticles are indicated to become slightly more stable after 44 days. This is observed as a 12% increase of the absorbance measured at λ_{max} and a lowering of the FWHM. The sharpening of the LSP peak and the increase of intensity measured at λ_{max} may be caused by annealing of Ag nanoparticle lattice defects, which is a slow process. Conversely, when NaCl is added during the synthesis significant aggregation occurs within 5 days. This is reflected by the fact that the absorbance intensity measured at λ_{max} decreases to 19% of the initial value. As λ_{max} is positioned at ~400nm, which is the position of λ_{max} of isolated Ag nanoparticles, it means that isolated nanoparticles are depleted from the solution, and this is probably caused by aggregation[21]. In comparison, the Ag nanoparticles with NaCl added after the synthesis are relatively stable as the intensity at λ_{max} decreases marginally to 93% of the initial value in 42 days (data not shown). However, this marginal aggregation with time may be caused by the fact that the sample was diluted for the absorbance measurement on the day of production, and that the spectra obtained the following days were obtained from this diluted sample. That is, during the 42 day period the NaCl concentration was only 6.67mM compared to 20mM in the sample with NaCl added during synthesis. Since the electric double layer repulsion decreases at increasing salt concentration this may explain why the particles with NaCl added after the particle synthesis are more stable with time than those with NaCl added during the synthesis.

In summary, the Ag nanoparticles synthesized without NaCl appears to be polydisperse and stable with time, while the particles with NaCl added during the synthesis appears monodisperse and unstable with time. The dispersity of the particles with NaCl added after the synthesis is intermediate to the dispersities of the particles without NaCl and the particles with NaCl added during synthesis. Minor aggregation occurred to the particles with NaCl added after the synthesis.

4.1.1 Stabilization with ATP or pto-ATP

Stabilization of Ag nanoparticles by adsorption of nucleobases and their derivatives is a relatively new approach[67]. According to Basu *et al.* (2008) the addition of adenine to Ag nanoparticles after their synthesis causes aggregation of the particles, which can be observed as a decrease of the plasmon peak at ~400nm and the presence of a red-shifted peak originating from the LSP of the aggregated nanoparticles[66]. In contrary to the results of Basu *et al.* (2008), it was found by Wei *et al.* (2007) that adenine stabilizes Ag nanoparticles when added during the particle synthesis, though at a concentration ~290 times higher than that used by Basu *et al.*[67]. It has been shown that stabilization of Au nanoparticles with ATP is better than with adenine[68], and efficient stabilization of Au nanoparticles with ATP has been obtained (data not shown). Therefore the same effect may be expected with Ag nanoparticles. The more efficient stabilization with ATP is caused by additional electrostatic stabilization due to the multivalent anionic character of this molecule. However, when ATP is added during the Ag nanoparticle synthesis the LSP peak is more asymmetric than when no ATP is added, and additionally the intensity at λ_{max} decreases, as observed from the results. These two factors both indicate initially a higher polydispersity of the ATP stabilized particles. Though, with time the LSP peak of the ATP stabilized particles red-shifts, narrows, and becomes more symmetric, and within one day the FWHM of the peak is smaller than that of unstabilized Ag nanoparticles. The intensity measured at λ_{max} of the ATP stabilized Ag nanoparticle peak increases by 24% within 44 days. As was observed with unstabilized particles, this may indicate the annealing of lattice defects. Though, with ATP present an additional process is observed, namely rearrangement of ATP on the nanoparticle surface. It may also indicate that the ATP stabilization becomes more effective with time, whereby flocculated Ag nanoparticles are stabilized and dissociate. However, the optimization of ATP stabilization alone probably occurs within a shorter time period than 44 days, wherefore the defect annealing is more likely.

When 20mM NaCl is added to the Ag nanoparticles with ATP added during particle synthesis, the particle solution is indicated to become significantly more monodisperse, as the FWHM of the LSP peak decreases by ~50% and the peak becomes symmetric. However, the particles are stable for at least 5 days, but within 42 days the intensity measured at λ_{max} decreases to 65% of the initial value, whereas λ_{max} is blue-shifted by 2nm and the FWHM decreases by 4nm (data not shown). That is, the presence of NaCl destabilizes the solution with time and causes particle aggregation. Similar decreases in stability were not observed for Ag nanoparticles with ATP added during the synthesis or particles with NaCl added after the synthesis, though theses samples were also more polydisperse. An explanation might be that the increased ionic strength due to NaCl addition is able to provide partial screening of the charges of the ATP. Thereby the electrostatic repulsion between the ATP molecules is decreased, and this enables adsorption of more ATP on the Ag nanoparticles, whereby the monodispersity is increased. Though, as was observed when NaCl was added to Ag nanoparticles without ATP present the increased salt concentration eventually results in aggregation.

Addition of ATP to Ag nanoparticles after the particle synthesis is observed, from the intensity measured at λ_{max} and the increased FWHM, to destabilize the particles slightly with time, when compared to unmodified particles. The shoulder present at ~450nm in the absorbance spectrum of the particles indicates the presence of aggregates[66]. This is contrary to the effect of ATP addition during the nanoparticle synthesis, as this entailed an initial destabilization followed by stabilization with time. When NaCl is added to the particles, the solution becomes more monodisperse, though the effect is still more significant when the

ATP is added during the nanoparticle synthesis. However, the stability with time is higher when ATP is added to the nanoparticles with NaCl after the synthesis, as the intensity measured at λ_{max} only decreases to 87% of the initial value in 42 days compared to 65% when ATP is added during the synthesis (data not shown). When NaCl was added after the synthesis to particles without ATP the decrease in intensity measured at λ_{max} was 7%, meaning that with time the simultaneous presence of ATP and NaCl entails higher destabilization of Ag nanoparticles than NaCl alone.

Stabilization of Ag nanoparticles with pto-ATP was expected to be more efficient than with ATP, as pto-ATP is anticipated to bind specifically to Ag through the phosphorothioate group[57]. However, addition of pto-ATP during Ag nanoparticle synthesis is observed to cause complete aggregation of the particles, which is evident from the lack of an LSP peak in the nanoparticle absorbance spectrum. When pto-ATP is added after the nanoparticle synthesis the particles are also destabilized and aggregation occurs. This is observed from the decrease in intensity at λ_{max} and the increase of FWHM as the LSP peak becomes increasingly asymmetric with time. Furthermore, the presence of aggregates that grow with time is indicated by the shoulder in the absorbance spectrum, which red-shifts with time. Addition of NaCl to this sample entails a small decrease of the FWHM of the LSP peak, though the very small decrease in aggregation indicated by this decrease may be considered irrelevant.

That is, pto-ATP destabilizes the Ag nanoparticle solutions both when added during or after the synthesis. Though, when added after the synthesis the process of destabilization progresses slower. This may again be caused by a lower adsorption of pto-ATP on the nanoparticles when it is added after the particle synthesis. In comparison, the addition of ATP during Ag nanoparticle synthesis causes an initial particle destabilization followed by stabilization with time, while addition of ATP after the synthesis causes destabilization with time. The simultaneous presence of ATP and NaCl is observed to initially improve the Ag nanoparticle dispersity, though with time the particles are destabilized more than with NaCl alone. In conclusion, it appears that the presence of a phosphorothioate group on ATP reduces the stabilizing ability of the molecule.

4.1.2 Binding of hp-DNA to ATP or pto-ATP Modified Ag Nanoparticles

To facilitate linking of the ATP or pto-ATP modified Ag nanoparticles to an Au surface, as proposed for the IL-4 binding assay, binding of DNA to the nanoparticles is necessary. For this purpose hp-DNA was chosen as a model oligonucleotide. The binding of hp-DNA entailed a decrease in stability of unmodified Ag nanoparticles and particles with ATP added during or after the particle synthesis, which was observed as a decrease of the intensities at λ_{max} and widening of the LSP peaks. The highest stability of the DNA modified particles is observed for particles with ATP added during the synthesis, which might also be expected as these particles also seemed to be the most stable before hp-DNA addition. The particles with pto-ATP added during the particle synthesis appears to aggregate further, whereas those with pto-ATP added after the particle synthesis are not affected at all, which might indicate that the hp-DNA does not bind to these particles.

The binding of hp-DNA to the nanoparticles was expected to improve the stability of the particles due to the increased charging of the nanoparticles at DNA binding. Thereby electrostatic repulsion between the particles is increased. Furthermore, steric stabilization of the particles might also be expected due to the possible extension of the oligonucleotides

from the particle surfaces. These effects are however not apparent and one reason may be that the hp-DNA was deprotected at the binding to the nanoparticles, which means that a free thiol group was present at the 5' end of the DNA. Despite the fact that DNA-Ag nanoparticle conjugates formed by binding of thiol-modified DNA are reported to be unstable, the free thiol group in hp-DNA may enable cross-linking of the hp-DNA modified particles[6,69]. This aggregation may be what causes the widening of the LSP peaks when hp-DNA is added.

4.1.3 Stabilization with DNA

Instead of attempting to stabilize Ag nanoparticles with ATP or pto-ATP and following bind DNA to the particles to produce conjugates another approach has been investigated. This approach is based on the use of the conjugated DNA as stabilizing agent, which has been proven possible in several cases[6,69,70]. It has the advantage of only requiring one step compared to the two steps required in the other approach. The Ag nanoparticles chosen for the stabilization were synthesized with NaCl added during the synthesis, as these particles are indicated to be more monodisperse than particles synthesized without NaCl or with NaCl added after the synthesis. The stabilization was attempted with four different DNA strands, namely r-DNA, hp-DNA, FAM-hp-DNA, and pto-DNA, and all four strands improve the stability of the Ag nanoparticles. This is evident as the intensities measured at λ_{max} of the samples heated with DNA present are higher than that of Ag nanoparticles that were heated without DNA. The heating was done in order to accelerate the DNA-nanoparticle conjugation process, as the collision frequency between nanoparticles and DNA is increased at elevated temperatures[71]. As might be expected, the extent of stabilization depends on the type and concentration of the DNA used. Generally, the use of a higher DNA concentration entails higher stability of the Ag nanoparticles, as deduced from the intensities measured at λ_{max}. This may also be expected as a higher concentration of DNA results in a higher collision frequency between DNA and nanoparticles. The binding of the DNA strands on the Ag nanoparticle surfaces is indicated by the red-shifted λ_{max} of the particles with DNA when compared to unheated particles[12]. However, the red-shift may also be caused by the heating as λ_{max} of heated particles without DNA is also red-shifted compared to unheated particles. Furthermore, the LSP peak of the Ag nanoparticles is observed to remain symmetric when DNA is added though the FWHM value increases at the addition. The intact symmetry of the peak indicates that the nanoparticle solutions are still monodisperse after DNA addition.

Of the four DNA strands used for the stabilization it appears that r-DNA provides the poorest stabilizing effect, which is predictable as this DNA strand contains no specific binding sites for the Ag nanoparticles. It may be speculated that the negatively charged phosphate groups in the DNA backbone prevents adsorption of the DNA at the negatively charged nanoparticles. However, the r-DNA is single stranded and does not form any stable secondary structures or homo-dimers. Therefore, it is probably able to uncoil sufficiently to expose the bases to the Ag surface and retain a sufficiently large distance between the phosphate groups and the surface[72]. That is, the interaction between r-DNA and Ag nanoparticles is non-specific and it is likely to occur through the functional groups of the nucleotide bases[12,66]. According to Basu *et al.* (2008), the strength of the interactions between nucleotide bases and Ag increases in the order thymine < adenine < guanine < cytosine, with the low strength of thymine binding being caused by lack of an exocyclic nitrogen[66]. Binding through the exocyclic nitrogen occurs due to the presence of an available electron lone pair[66,73]. The poorest stabilizing effect provided by r-DNA compared to the other three strands is also confirmed by agarose gel electrophoresis, as r-DNA

stabilized Ag nanoparticles are not able to enter the gel and aggregates instead. The aggregation may either be caused by the relatively high ionic strength in the 1X TBE buffer used for the electrophoresis or by stripping of the DNA from the surface when voltage is applied. In both cases the aggregation is entailed by lowering of the electrostatic repulsion between the nanoparticles. When the other three DNA strands were used for stabilization the Ag nanoparticles migrated in the gel and formed bands. Hereby it is inferred that these three strands are not bound to Ag nanoparticles solely by non-specific interactions.

Stabilization of Ag nanoparticles with ATP was also attempted using the same approach as for DNA stabilization in order to be able to compare the ATP and DNA stabilization effects. A minor stabilizing effect of ATP was observed when compared to heated Ag nanoparticles, though the effect was lower than that from r-DNA (data not shown). The agarose gel electrophoresis confirms that the ATP stabilized Ag nanoparticles are not more stable than the r-DNA stabilized ones, as neither of them migrate in the gel. It might be anticipated that the adsorption of ATP was supposed to provide higher stability than that of r-DNA, as the adsorption rate of ATP is expected to be higher due to the requirement of energetically unfavourable uncoiling at binding of r-DNA[71]. Each r-DNA molecule carries 30 negative charges, whereas each ATP molecule carries 3 or 4 negative charges and furthermore ATP is present at a concentration 10 times higher than that of r-DNA. Therefore the numbers of charges available for stabilization in the ATP and r-DNA containing samples are approximately equal. Hence, the indicated higher stability of r-DNA stabilized particles is likely to originate from more efficient adsorption of r-DNA. This may be due to the presence of more adsorption sites per negative charge in r-DNA compared to ATP.

Determined from the intensities measured at λ_{max} of the Ag nanoparticle absorbance spectra, FAM-hp- and hp-DNA both provide higher stability than r-DNA. This is most likely to be caused by the presence of phosphorothioate groups at the backbone in the loop region of these DNA strands. Hereby, specific binding sites for the Ag nanoparticles are provided, and this is indicated to provide a stronger binding to the nanoparticles than the non-specific binding observed with r-DNA[57]. The double stranded region in FAM-hp- and hp-DNA with a Tm of 92.7°C is not expected to bind non-specifically to Ag nanoparticles, as the nucleotide bases are involved in Watson-Crick base pairing[72]. Hence, the sites for non-specific binding are not available. That is, the DNA probably extends from the nanoparticle surface whereby steric stabilization is also provided in addition to the electrostatic stabilization. From the intensities at λ_{max} and the weaker band of FAM-hp-DNA stabilized particles observed in the agarose gel it is furthermore indicated that hp-DNA provides higher stability than FAM-hp-DNA. That is, the presence of the FAM fluorophore, instead of the protected thiol, at the 5' end of the hairpin structure partly inhibits the binding of the DNA or the presence of the protected thiol increases the binding.

The best DNA strand for Ag nanoparticle stabilization among the four tested ones appears to be pto-DNA. This is inferred from the fact that pto-DNA stabilized Ag nanoparticles form the clearest band at agarose gel electrophoresis and that the absorbance spectra of these particles exhibit the highest intensity measured at λ_{max} among all the samples. As the strand does not form secondary structures or homo-dimers, whereby uncoiling is not inhibited, and as phosphorothioate groups for specific binding to Ag are present at the DNA backbone, this may also be expected[57,72]. Doubling of the pto-DNA concentration is observed not to increase the particle stability significantly, which may indicate that the maximum possible stabilization of the Ag nanoparticles is obtained with

2.86μM pto-DNA. Hence, a further increase of the pto-DNA concentration may not increase the particle stability further.

In 5 days considerable aggregation of the unheated Ag nanoparticles is observed, which is indicated by the decrease in λ_{max} of the absorbance spectra. In contrary, no decreases larger than 17% appears in the intensities at λ_{max} of the DNA stabilized particles within 22 days. That is, the DNA stabilized particles also appear to be relatively stable with time. The FWHM and λ_{max} of the particles stabilized with 1.43 or 2.86μM pto-DNA or with 2.86μM hp-DNA do not change in 22 days. This may indicate that these samples are particularly stable, as was also interpreted from the intensities at λ_{max}. The FWHM and λ_{max} of the remaining samples all decrease, which may indicate that there is a preference for the larger Ag nanoparticles to aggregate first in these samples.

The stabilization of Ag nanoparticles with DNA has shown that specific binding of DNA to Ag nanoparticles through phosphorothioate groups is possible and that this improves the DNA binding significantly compared to non-specific binding.

4.2 SPR Based IL-4 Binding Assay

Once stabilization and conjugation with DNA of Ag nanoparticles has been achieved the particles may be further used in the SPR based IL-4 binding assay proposed in the beginning of this report.

Binding of Ag nanoparticles to an Au surface by use of a double stranded DNA linker has been examined with two different DNA linkers, namely the hp-DNA hairpin structure and the hetero-dimer formed by thiol- and pto-DNA. As appears from AFM imaging the binding of hp-DNA modified Ag nanoparticles entailed a particle density of 3.25particles/μm^2 on a flame annealed Au surface, whereas binding with the thiol-/pto-DNA dimer entailed a density of 569particles/μm^2. The reason for the very low density of bound hp-DNA modified particles may be that excess DNA was not removed by centrifugation before the immobilization. Hence, DNA that is not conjugated to Ag nanoparticles may then bind on the surface and repel the conjugates. However, estimated from the AFM imaging the surface concentration of non-conjugated DNA is not very high and therefore this is not expected to be the only reason for the low binding of the conjugates. Another reason may be that the hp-DNA was not deprotected, and therefore no free thiols were available for binding to the Au surface. The thiol-Ag interaction has been reported to be weaker than the thiol-Au interaction[69]. However, despite its weaker character the thiol-Ag interaction may still occur if the hp-DNA is deprotected, which might lead to nanoparticle aggregation instead of linking to the Au surface. The binding of hp-DNA stabilized Ag nanoparticles to the Au surface is therefore relying on the ability of the disulphide to bind to the Au surface. Binding of disulphide-terminated oligonucleotides to Au nanoparticles has been reported, though as inferred from the very low density of bound hp-DNA modified Ag nanoparticles it is unlikely to occur to the Au surface used in this case[69].

In the first step of binding Ag nanoparticles to an Au surface with thiol-/pto-DNA dimers the thiol-DNA was linked to the Au surface. Binding of the DNA on the Au surface was confirmed by an increase in the SPR spectrophotometer signal, which means that the resonance angle of the surface plasmons at the Au surface increases. However, the increases observed in the experiment for binding of dsDNA and the experiment for binding of pto-DNA modified Ag nanoparticles were not identical, with the response being largest in the first experiment. This may e.g. be caused by variations between the Au surfaces used in the two experiments, which may be caused by uncertainties in the surface production method.

To maximize the amount of thiol-DNA bound on the surface the DNA was dissolved in buffer of high ionic strength. This was done in order to minimize the electrostatic repulsion between the DNA molecules binding to the Au surface[61]. In the second step of the binding process the Au surface was exposed to mercaptohexanol. Mercaptohexanol has been reported to dissociate non-specifically bound DNA from the surface and create a monolayer on the surface which ensures that the specifically bound DNA extends away from the surface[61,74,75]. The non-specifically bound DNA is expected to be bound to the Au surface through interaction with the nucleotide bases, as was also expected with Ag nanoparticles[61]. Furthermore, the lengths of mercaptohexanol and the 5' thiol linker of thiol-DNA are equal, which means that the mercaptohexanol is not expected to interfere with the later DNA hybridization. Due to the dissociation of DNA and the formation of a mixed monolayer in the sample chamber compared to the formation of a full monolayer in the reference chamber the signal increase is expected to be highest in the reference chamber at mercaptohexanol binding. Though, owing to the small size of mercaptohexanol compared to the DNA molecules and an expected relatively low concentration of DNA on the surface the signal difference is anticipated to be small. However, in both experiments the signal increase was observed to be highest in the sample chamber.

Hybridization of pto-DNA with the bound thiol-DNA was observed in the SPR sample chamber, whereas no binding was observed in the reference chamber, as was indicated by the fact that only the signal of the sample chamber increased when pto-DNA was injected. This indicates that the pto-DNA is not able to bind to the mercaptohexanol layer, as has also been reported by Herne and Tarlov (1997)[61]. Therefore it may also be anticipated that the binding in the sample chamber proceeds by hybridization of the two complementary DNA strands and not by non-specific interactions to the mercaptohexanol layer.

Hybridization of pto-DNA bound to Ag nanoparticles with thiol-DNA at the Au surface caused an increase in the SPR signal 18 times higher than the hybridization of pto-DNA. That is, the presence of Ag nanoparticles causes a massive increase of the surface plasmon resonance angle, as might also be expected. However, in contrary to what was observed at binding of pto-DNA, the binding of pto-DNA modified Ag nanoparticles also causes an increase of the reference chamber signal. That is, non-specific binding of the nanoparticles to the mercaptohexanol monolayer is indicated. Additionally, it is observed that flushing of the surface with 500mM NaCl does not dissociate the non-specifically bound nanoparticles. Furthermore, the reflectivity at the resonance angle increases at Ag nanoparticle binding, which was not observed at pto-DNA binding. According to Mock *et al.* (2008), the SPP resonance condition in an infinite thin Au film is insignificantly perturbed by the presence of a single Au nanoparticle above the film[15]. However, in our experiment the Ag nanoparticle density on the Au surface is expected to be high, as inferred from AFM imaging, whereby the perturbation may become significant. According to theory, the resonance angle is affected by changing the dielectric permittivity at the metal surface, whereas the reflectivity at the resonance angle is not affected by dielectric permittivity changes. Hence, the change in reflectivity at the resonance angle is caused by the Ag nanoparticles, and the change may be due to scattering of the metal film surface plasmons by the nanoparticles. However, attenuation of the metal film SPP by nanoparticle scattering is also expected to increase the width of the reflectivity dip, though this is not clearly observed[38].

4.2.1 Binding of IL-4 to dsDNA

Binding of IL-4 to the thiol-/pto-DNA dimer linked to an Au surface yielded association and dissociation rate constants of $432 M^{-1}s^{-1}$ and $0.00002 s^{-1}$ at the first injection of 7.5µM IL-4 and $256 M^{-1}s^{-1}$ and $0.00002 s^{-1}$ at the second injection, respectively. In comparison, Hsu *et al.* (2005) obtained association and dissociation rate constants of $761 M^{-1}s^{-1}$ and $0.146 s^{-1}$, respectively, for binding of IL to hairpin structured DNA with the sequence 5'-C[GT]$_4$CCCC[AG]$_4$G-3'[46]. That is, the binding of IL-4 to dsDNA is indicated to be slower than that of IL, though when bound, IL-4 appears to interact stronger with the DNA than does IL. According to literature the antibacterial activity of IL-4 is lower than that of IL, which correlates well with the result that IL-4 binding to DNA is slower than IL binding[48]. The lowest concentration of IL-4 detected at binding to the thiol-/pto-DNA dimer was 0.1µM. However, the data are fairly noisy and association rate constant determined from the binding curve deviates by two orders of magnitude from those obtained from the 7.5µM injections. Therefore more experiments are necessary to be able to compare it with the remaining results.

The association and dissociation rate constants obtained for the binding of 7.5µM IL-4 to the thiol-/pto-DNA dimer interlinking an Au surface and Ag nanoparticles were found to be $252 M^{-1}s^{-1}$ and $0.0001 s^{-1}$ for the first injection, respectively, and $217 M^{-1}s^{-1}$ and $0.00004 s^{-1}$ for the second injection. This is in agreement with the association rate constants determined without Ag nanoparticles present, whereas the dissociation rate constant is indicated to be higher at the binding of IL-4 to dsDNA interlinking Au surface and Ag nanoparticles. The faster dissociation may be caused by binding of IL-4 to the single stranded pto-DNA stabilizing the bound Ag nanoparticles and adsorption of the cationic peptide on the negatively charged Ag particles. The binding to ssDNA and the adsorption to the nanoparticles are both expected to be weaker than the binding to dsDNA, which explains why the observed effective dissociation rate constant is higher when Ag nanoparticles are linked to the dsDNA[46]. When comparing the Rmax values determined without and with Ag nanoparticles bound to the dsDNA it appears that the presence of the nanoparticles decreases the binding of IL-4. This may however be caused by a lower density of dsDNA at the Au surface when the dsDNA is linked to the Ag nanoparticles, as the DNA with nanoparticles occupy a significantly larger area at the Au surface compared to dsDNA alone. According to AFM imaging the particle sizes of pto-DNA modified particles linked to a flame annealed Au surface and an Au surface used for SPR spectroscopy are 16.5±3.1 and 15.3±4.2nm, respectively. Hence, the dsDNA density at the Au surface is reduced due to steric hindrance when Ag nanoparticles are present. In contrary, it was expected that the nanoparticle scattering of the metal film surface plasmons would be sensitive to the metal film-nanoparticle distance[15], and that IL-4 would change this distance due to conformational changes in the DNA upon IL-4 binding. Hereby, the binding of IL-4 to dsDNA might be expected to be observable as a change in the width of the reflectivity dip in the reflectivity scans from the metal film[38]. However, no significant change in the appearance of the reflectivity scan was observed upon IL-4 binding. This may be caused by the distance between the Au surface and the Ag nanoparticles being too large, whereby the nanoparticle-SPP interaction may not be strong enough to be observed. Though, it may also be caused by the DNA conformational change entailed by IL-4 binding being too small. The sensitivity may be optimized by using a wavelength for SPP excitation, which is closer to the wavelength of the nanoparticle LSP.

In order to dissociate IL-4 from dsDNA by screening of the electrostatic interactions between the cationic IL-4 and the anionic DNA 0.5M NaCl was used. From the decrease of

the SPR signal upon the NaCl injection it may be interpreted that the dissociation is successful. However, after the dissociation of 0.1μM IL-4 bound to dsDNA without Ag nanoparticles present (data not shown) and of 7.5μM IL-4 bound to dsDNA with nanoparticles present in the second injection further binding of IL-4 was not possible. The SPR signal was not observed to decrease to the same level as before pto-DNA or pto-DNA modified particles were injected, wherefore it is not likely that the thiol- and pto-DNA dissociate from thiol-DNA. Neither is it probable that the entire dsDNA structures dissociate due to the breakage of the Au-thiol linkage. This indicates that further optimization of the process is necessary, and it may probably involve other components such as detergents.

5 Conclusion

The objective of this project may be split into two parts. One part was aimed at the development of methods for stabilization of Ag nanoparticles and for production of DNA-Ag nanoparticle conjugates. The other part was aimed at linking of the DNA-Ag nanoparticle conjugates to an Au film in order to produce a biosensor based on the scattering of the film SPPs by the nanoparticles.

We have compared the stabilizing effects of Ag nanoparticles stabilized with mononucleotides and short DNA strands, which were both phosphorothioated and not. Optimum stabilization and DNA-nanoparticle conjugation was obtained with phosphorothioated ssDNA. The stabilization and conjugation process lasted only 2 hours and required heating of the DNA-nanoparticle solution to 60°C. The most narrow size distribution of the used Ag nanoparticles was obtained by adding 20mM NaCl during the particle synthesis. Conjugation of Ag nanoparticles with hairpin structured DNA modified with phosphorothioate groups in the loop region was also able to provide significant Ag nanoparticle stabilization. However, the stabilization with hairpin structured DNA was less efficient than with phosphorothioated ssDNA. This was probably due to less non-specific interactions between the double stranded hairpin DNA and the nanoparticles. The stabilizing effects of both types of phosphorothioated DNA were superior to the effect of random sequenced ssDNA which was not phosphorothioated.

It was also attempted to stabilize Ag nanoparticles with phosphorothioated ATP. Though, contradictory to what was expected, it was found that the presence of the phosphorothioate group reduced the stabilizing ability of the molecule and instead made it cause nanoparticle aggregation.

In the last part of the project we compared the sensitivity of a SPP based SPR assay involving the DNA binding peptide IL-4 and either dsDNA or dsDNA-Ag nanoparticle conjugates. A larger shift of the SPP resonance angle was observed at 7.5μM IL-4 binding to dsDNA compared to binding to dsDNA-Ag nanoparticle conjugates. This was probably caused by a lower DNA density when the DNA was linked to nanoparticles compared to without nanoparticles. Furthermore, a shift of the width of the Au film reflectivity dip was expected at IL-4 binding to dsDNA-Ag nanoparticle conjugates due to a changed nanoparticle-film distance and thereby a changed nanoparticle-SPP interaction. This was though not clearly observed, which might be caused by a too large nanoparticle-film distance, a too small conformational change of the DNA at IL-4 binding, or use of a too long wavelength for SPP excitation. For the binding of IL-4 to dsDNA association and dissociation rate constants of $432M^{-1}s^{-1}$ and $0.00002s^{-1}$ were obtained, whereas those obtained for IL-4 binding to dsDNA-Ag nanoparticle conjugates were $252M^{-1}s^{-1}$ and $0.0001s^{-1}$, respectively. The higher dissociation rate constant in the latter case may be caused by a weaker binding of IL-4 to Ag nanoparticles and to ssDNA bound to the particles.

6 Future Perspectives

On the basis of the results obtained in this study additional experiments may be proposed. In some cases it was found that Ag nanoparticle polydispersity and aggregation were not distinguishable from the obtained absorbance spectra. Therefore other techniques such as dynamic light scattering, AFM imaging, and transmission electron microscopy imaging for determination of particle sizes and distributions may be used. Hereby the ambiguity of the absorbance spectra would be removed.

It was observed that the addition of NaCl during Ag nanoparticle synthesis and the addition of NaCl to ATP stabilized particles provided a more narrow size distribution of the nanoparticles. However, the presence of the NaCl was also observed to cause particle aggregation with time. It may be envisaged that removal of the NaCl e.g. by dialysis against a buffer of lower ionic strength may prevent the aggregation of the narrowly distributed particle solution. Furthermore, it may be used to homogenise the ionic strength of samples that are to be compared.

The SPP based SPR binding assay for detection of IL-4 binding to dsDNA or dsDNA-Ag nanoparticle conjugates was observed to have a higher sensitivity without the nanoparticles present. In order to increase the sensitivity of the SPP-nanoparticle interaction without changing the DNA length it may be suggested to tune the SPP resonance wavelength to the LSP resonance wavelength. Thereby it is expected that the nanoparticle scattering of the SPP would be increased due to the SPP-LSP coupling. The sensitivity may also be increased by measuring the LSP scattering instead of the metal film reflectivity[15]. However, this would require a new experimental setup similar to the one used by Mock *et al.* (2008) in which the nanoparticle scattering is monitored by use of dark-field microscopy.

Furthermore, no conductivity measurements have been performed on the DNA-nanoparticle conjugates linked to the metal film. When this is done it may aid to solve the controversies about the DNA conductivity issue in order to determine the applicability of DNA for molecular electronics.

7 Bibliography

1. Maier, S. A. (2007). "*Plasmonics: Fundamentals and Applications*", Springer.
2. Homola, J. (2008). "*Surface plasmon resonance sensors for detection of chemical and biological species*". Chemical Reviews **108**(2): 462-493.
3. Sepulveda, B., P. C. Angelome, L. M. Lechuga and L. M. Liz-Marzan (2009). "*LSPR-based nanobiosensors*". Nano Today **4**(3): 244-251.
4. Biacore. http://www.biacore.com/lifesciences/technology/introduction/following_interaction/index.html. Date accessed 24-07-2009.
5. Reichert. www.reichertspr.com. Date accessed 24-07-2009.
6. Lee, J. S., A. K. R. Lytton-Jean, S. J. Hurst and C. A. Mirkin (2007). "*Silver nanoparticle-oligonucleotide conjugates based on DNA with triple cyclic disulfide moieties*". Nano Letters **7**(7): 2112-2115.
7. Mirkin, C. A., R. L. Letsinger, R. C. Mucic and J. J. Storhoff (1996). "*A DNA-based method for rationally assembling nanoparticles into macroscopic materials*". Nature **382**(6592): 607-609.
8. Alivisatos, A. P., K. P. Johnsson, X. G. Peng, T. E. Wilson, C. J. Loweth, M. P. Bruchez and P. G. Schultz (1996). "*Organization of 'nanocrystal molecules' using DNA*". Nature **382**(6592): 609-611.
9. Radziuk, D., D. G. Shchukin, A. Skirtach, H. Mohwald and G. Sukhorukov (2007). "*Synthesis of silver nanoparticles for remote opening of polyelectrolyte microcapsules*". Langmuir **23**(8): 4612-4617.
10. Nehl, C. L. and J. H. Hafner (2008). "*Shape-dependent plasmon resonances of gold nanoparticles*". Journal of Materials Chemistry **18**(21): 2415-2419.
11. Jain, P. K., W. Y. Huang and M. A. El-Sayed (2007). "*On the universal scaling behavior of the distance decay of plasmon coupling in metal nanoparticle pairs: A plasmon ruler equation*". Nano Letters **7**(7): 2080-2088.
12. Thompson, D. G., A. Enright, K. Faulds, W. E. Smith and D. Graham (2008). "*Ultrasensitive DNA detection using oligonucleotide-silver nanoparticle conjugates*". Analytical Chemistry **80**(8): 2805-2810.
13. Cao, Y. W., R. Jin and C. A. Mirkin (2001). "*DNA-modified core-shell Ag/Au nanoparticles*". Journal of the American Chemical Society **123**(32): 7961-7962.
14. Tombelli, S., M. Minunni and M. Mascini (2002). "*A surface plasmon resonance biosensor for the determination of the affinity of drugs for nucleic acids*". Analytical Letters **35**(4): 599-613.
15. Mock, J. J., R. T. Hill, A. Degiron, S. Zauscher, A. Chilkoti and D. R. Smith (2008). "*Distance-dependent plasmon resonant coupling between a gold nanoparticle and gold film*". Nano Letters **8**(8): 2245-2252.
16. Tokareva, I., S. Minko, J. H. Fendler and E. Hutter (2004). "*Nanosensors based on responsive polymer brushes and gold nanoparticle enhanced transmission surface plasmon resonance spectroscopy*". Journal of the American Chemical Society **126**(49): 15950-1.
17. Jensen, K. R. (2008). "A Preliminary Study for the Construction of DNA-Nanoparticle Conjugates: Building Blocks for DNA Molecular Electronics". Institute for Physics and Nanotechnology, Aalborg University, Aalborg. **8th semester project**
18. Barnes, G. T. and I. R. Gentle (2005). "*An introduction to interfacial science*". Oxford, Oxford University Press.
19. Lu, K. (2008). "*Theoretical analysis of colloidal interaction energy in nanoparticle suspensions*". Ceramics International **34**(6): 1353-1360.
20. Kvitek, L., A. Panacek, J. Soukupova, M. Kolar, R. Vecerova, R. Prucek, M. Holecova and R. Zboril (2008). "*Effect of surfactants and polymers on stability and antibacterial activity of silver nanoparticles (NPs)*". Journal of Physical Chemistry C **112**(15): 5825-5834.

21. Moskovits, M. and B. Vlckova (2005). "*Adsorbate-induced silver nanoparticle aggregation kinetics*". Journal of Physical Chemistry B **109**(31): 14755-14758.
22. Israelachvili, J. (1992). "*Intermolecular & Surface Forces*", Academic Press, 2nd edition.
23. Kim, T., K. Lee, M. S. Gong and S. W. Joo (2005). "*Control of gold nanoparticle aggregates by manipulation of interparticle interaction*". Langmuir **21**(21): 9524-9528.
24. Reitz, J. R., F. J. Milford and R. W. Christy (1993). "*Foundations of Electromagnetic Theory*", Addison-Wesley Publishing Company, Inc., 4th edition.
25. Hamaker, H. C. (1937). "*The London - Van Der Waals attraction between spherical particles*". Physica **4**: 1058-1072.
26. Ji, X. H., X. N. Song, J. Li, Y. B. Bai, W. S. Yang and X. G. Peng (2007). "*Size control of gold nanocrystals in citrate reduction: The third role of citrate*". Journal of the American Chemical Society **129**(45): 13939-13948.
27. Van Hyning, D. L. and C. F. Zukoski (1998). "*Formation mechanisms and aggregation behavior of borohydride reduced silver particles*". Langmuir **14**(24): 7034-7046.
28. Lewis, J. A. (2000). "*Colloidal processing of ceramics*". Journal of the American Ceramic Society **83**(10): 2341-2359.
29. Kittel, C. (2005). "*Introduction to Solid State Physics*". New Caledonia, John Wiley & sons, Inc.
30. Pitarke, J. M., V. M. Silkin, E. V. Chulkov and P. M. Echenique (2007). "*Theory of surface plasmons and surface-plasmon polaritons*". Reports on Progress in Physics **70**(1): 1-87.
31. Kooyman, R. P. H. (2008). "*Physics of Surface Plasmon Resonance*". Handbook of Surface Plasmon Resonance. R. B. M. Schasfoort and A. J. Tudos. Cambridge, The Royal Society of Chemistry**:** 15-34.
32. Yu, F. (2004). "Surface Plasmon Fluorescence Spectroscopy and Surface Plasmon Diffraction in Biomolecular Interaction Studies". Max-Planck-Institute für Polymerforschung, Johannes Gutenberg-Universität, Mainz. **Doktor der Naturwissenschaft**
33. Leveque, G. and O. J. F. Martin (2006). "*Tunable composite nanoparticle for plasmonics*". Optics Letters **31**(18): 2750-2752.
34. Raether, H. (1988). "*Surface Plasmons on Smooth and Rough Surfaces and on Gratings*", Springer-Verlag.
35. Klein, M. V. and T. E. Furtak (1986). "*Optics*", John Wiley & Sons, Inc., 2nd edition.
36. Sato, A. (2006). "Surface Plasmon Fluorescence Spectroscopy and Optical Waveguide Fluorescence Spectroscopy in Limit of Detection Studies". Max Planck Institute for Polymer Research, Johannes Gutenberg University of Mainz, Mainz. **Master thesis**
37. Johnson, P. B. and R. W. Christy (1972). "*Optical Constants of the Noble Metals*". Physical Review B **6**(12): 4370-4379.
38. Homola, J. (2006). "*Electromagnetic Theory of Surface Plasmons*". Surface Plasmon Resonance Based Sensors. J. Homola. Berlin, Springer-Verlag Berlin Heidelberg.
39. Ekgasit, S., C. Thammacharoen, F. Yu and W. Knoll (2004). "*Evanescent field in surface plasmon resonance and surface plasmon field-enhanced fluorescence spectroscopies*". Analytical Chemistry **76**(8): 2210-2219.
40. Scaffardi, L. B. and J. O. Tocho (2006). "*Size dependence of refractive index of gold nanoparticles*". Nanotechnology **17**(5): 1309-1315.
41. Link, S. and M. A. El-Sayed (1999). "*Size and temperature dependence of the plasmon absorption of colloidal gold nanoparticles*". Journal of Physical Chemistry B **103**(21): 4212-4217.
42. Nath, N. and A. Chilkoti (2004). "*Label free colorimetric biosensing using nanoparticles*". Journal of Fluorescence **14**(4): 377-389.
43. Hovel, H., S. Fritz, A. Hilger, U. Kreibig and M. Vollmer (1993). "*Width of Cluster Plasmon Resonances - Bulk Dielectric Functions and Chemical Interface Damping*". Physical Review B **48**(24): 18178-18188.
44. Pellegrini, G., G. Mattei, V. Bello and P. Mazzoldi (2007). "*Interacting metal nanoparticles: Optical properties from nanoparticle dimers to core-satellite systems*". materials Science and Engineering C **27**: 1347-1350.
45. Leveque, G. and O. J. F. Martin (2006). "*Optical interactions in a plasmonic particle coupled to a metallic film*". Optics Express **14**(21): 9971-9981.
46. Hsu, C. H., C. P. Chen, M. L. Jou, A. Y. L. Lee, Y. C. Lin, Y. P. Yu, W. T. Huang and S. H. Wu (2005). "*Structural and DNA-binding studies on the bovine antimicrobial peptide,*

indolicidin: evidence for multiple conformations involved in binding to membranes and DNA". Nucleic Acids Research **33**(13): 4053-4064.
47. Marchand, C., K. Krajewski, H. F. Lee, S. Antony, A. A. Johnson, R. Amin, P. Roller, M. Kvaratskhelia and Y. Pommier (2006). "*Covalent binding of the natural antimicrobial peptide indolicidin to DNA abasic sites*". Nucleic Acids Research **34**(18): 5157-5165.
48. Subbalakshmi, C., E. Bikshapathy, N. Sitaram and R. Nagaraj (2000). "*Antibacterial and hemolytic activities of single tryptophan analogs of indolicidin*". Biochemical and Biophysical Research Communications **274**(3): 714-716.
49. Kim, S. M., J. M. Kim, B. P. Joshi, H. Cho and K. H. Lee (2009). "*Indolicidin-derived antimicrobial peptide analogs with greater bacterial selectivity and requirements for antibacterial and hemolytic activities*". Biochimica Et Biophysica Acta-Proteins and Proteomics **1794**(2): 185-192.
50. Halevy, R., A. Rozek, S. Kolusheva, R. E. Hancock and R. Jelinek (2003). "*Membrane binding and permeation by indolicidin analogs studied by a biomimetic lipid/polydiacetylene vesicle assay*". Peptides **24**(11): 1753-61.
51. Subbalakshmi, C. and N. Sitaram (1998). "*Mechanism of antimicrobial action of indolicidin*". Fems Microbiology Letters **160**(1): 91-96.
52. Park, K. H., Y. Park, I. S. Park, K. S. Hahm and S. Y. Shin (2008). "*Bacterial selectivity and plausible mode of antibacterial action of designed Pro-rich short model antimicrobial peptides*". Journal of Peptide Science **14**(7): 876-882.
53. Owczarzy, R., A. V. Tataurov, Y. Wu, J. A. Manthey, K. A. McQuisten, H. G. Almabrazi, K. F. Pedersen, Y. Lin, J. Garretson, N. O. McEntaggart, C. A. Sailor, R. B. Dawson and A. S. Peek (2008). "*IDT SciTools: a suite for analysis and design of nucleic acid oligomers*". Nucleic Acids Research **36**: W163-W169.
54. Horcas, I., R. Fernandez, J. M. Gomez-Rodriguez, J. Colchero, J. Gomez-Herrero and A. M. Baro (2007). "*WSXM: A software for scanning probe microscopy and a tool for nanotechnology*". Review of Scientific Instruments **78**(1): -.
55. Gill, S. C. and P. H. Vonhippel (1989). "*Calculation of Protein Extinction Coefficients from Amino-Acid Sequence Data*". Analytical Biochemistry **182**(2): 319-326.
56. Zhao, W. T., T. M. H. Lee, S. S. Y. Leung and I. M. Hsing (2007). "*Tunable stabilization of gold nanoparticles in aqueous solutions by mononucleotides*". Langmuir **23**(13): 7143-7147.
57. Kotlyar, A. and T. Molotsky (2009). Production and Optical Properties of DNA-Nanoparticle Hybrids. Molecular Plasmonics, Jena, Germany.
58. Berg, J. M., J. L. Tymoczko and L. Stryer (2007). "*Biochemistry*", W. H. Freeman and Company, 6th edition.
59. Creighton, T. E. (1993). "*Proteins - Structures and Molecular Properties*". New York, W. H. Freeman and Company, 2nd edition.
60. Stepanek, J., H. Vaisocherova and M. Piliarik (2006). "*Molecular Interactions in SPR Sensors*". Surface Plasmon Resonance Based Sensors. J. Homola. Berlin, Springer-Verlag Berlin Heidelberg.
61. Herne, T. M. and M. J. Tarlov (1997). "*Characterization of DNA probes immobilized on gold surfaces*". Journal of the American Chemical Society **119**(38): 8916-8920.
62. Song, K. C., S. M. Lee, T. S. Park and B. S. Lee (2009). "*Preparation of colloidal silver nanoparticles by chemical reduction method*". Korean Journal of Chemical Engineering **26**(1): 153-155.
63. Radziuk, D., A. Skirtach, G. Sukhorukov, D. Shchukin and H. Mohwald (2007). "*Stabilization of silver nanoparticles by polyelectroliftes and poly(eithylene glycol)*". Macromolecular Rapid Communications **28**(7): 848-855.
64. Wang, W., S. Efrima and O. Regev (1998). "*Directing oleate stabilized nanosized silver colloids into organic phases*". Langmuir **14**(3): 602-610.
65. Kapoor, S. (1998). "*Preparation, characterization, and surface modification of silver particles*". Langmuir **14**(5): 1021-1025.
66. Basu, S., S. Jana, S. Pande and T. Pal (2008). "*Interaction of DNA bases with silver nanoparticles: Assembly quantified through SPRS and SERS*". Journal of Colloid and Interface Science **321**(2): 288-293.
67. Wei, H., J. Li, Y. L. Wang and E. K. Wang (2007). "*Silver nanoparticles coated with adenine: preparation, self-assembly and application in surface-enhanced Raman scattering*". Nanotechnology **18**(17).

68. Zhao, W. A., F. Gonzaga, Y. F. Li and M. A. Brook (2007). "*Highly stabilized nucleotide-capped small gold nanoparticles with tunable size*". Advanced Materials **19**(13): 1766-1771.
69. Dougan, J. A., C. Karlsson, W. E. Smith and D. Graham (2007). "*Enhanced oligonucleotide-nanoparticle conjugate stability using thioctic acid modified oligonucleotides*". Nucleic Acids Research **35**(11): 3668-3675.
70. Vidal, B. C., T. C. Deivaraj, J. Yang, H. P. Too, G. M. Chow, L. M. Gan and J. Y. Lee (2005). "*Stability and hybridization-driven aggregation of silver nanoparticle-oligonucleotide conjugates*". New Journal of Chemistry **29**(6): 812-816.
71. Li, H. X. and L. J. Rothberg (2004). "*Label-free colorimetric detection of specific sequences in genomic DNA amplified by the polymerase chain reaction*". Journal of the American Chemical Society **126**(35): 10958-10961.
72. Li, H. X. and L. Rothberg (2004). "*Colorimetric detection of DNA sequences based on electrostatic interactions with unmodified gold nanoparticles*". Proceedings of the National Academy of Sciences of the United States of America **101**(39): 14036-14039.
73. Otto, C., F. F. M. de Mul, A. Huizinga and J. Greve (1988). "*Surface Enhanced Raman Scattering of Derivatives of Adenine. The Importance of the External Amino Group in Adenine for Surface Binding*". Journal of physical Chemistry **92**: 1239-1244.
74. Park, S., K. A. Brown and K. Hamad-Schifferli (2004). "*Changes in oligonucleotide conformation on nanoparticle surfaces by modification with mercaptohexanol*". Nano Letters **4**(10): 1925-1929.
75. Mbindyo, J. K. N., B. D. Reiss, B. R. Martin, C. D. Keating, M. J. Natan and T. E. Mallouk (2001). "*DNA-directed assembly of gold nanowires on complementary surfaces*". Advanced Materials **13**(4): 249-254.

A Appendix: Chemicals

Adenosine 5'-triphosphate, disodium salt (ATP) (Sigma, CAS-nr.: 987-65-5); Adenosine 5'-[γ-thio]triphosphate tetralithium salt (pto-ATP) (Sigma, CAS-nr.: 93839-89-5); DL-Dithiothreitol (DTT) (Sigma, CAS-nr.: 3483-12-3); Ethylenediaminetetraacetic acid (EDTA) (Sigma, CAS-nr.: 60-00-4); Ethylene glycol (Riedel-de Haën; CAS-nr.: 107-21-1); Formic acid 98-100% (Merck, Cat-nr.: 1.00264.0100); Hydrochloric acid 37% (HCl) (Merck, Cat-nr.: 1.00317.2500); Silver nitrate ($AgNO_3$) (Sigma, CAS-nr.: 7761-88-8); Sodium citrate tribasic dihydrate (Sigma, CAS-nr.: 6132-04-3); Sodium Borohydride ($NaBH_4$) (Aldrich, CAS-nr.: 16940-66-2); Sodium chloride (NaCl) (Sigma-Aldrich, CAS-nr.: 7647-14-5); Sodium hydroxide (NaOH) (Bie & Berntsen, Batch-nr.: 4228203); Sodium phosphate, dibasic heptahydrate (Sigma-Aldrich, CAS-nr.: 7782-85-6); Sodium phosphate, monobasic (Sigma-Aldrich, CAS-nr.: 7558-80-7); Trifluoroacetic acid (TFA) (Irish Biotech GmbH, CAS-nr.: 76-05-1); Tris[hydroxymethyl]aminomethane (Tris) (Sigma, CAS-nr.: 77-86-1); UltraPure™ 10X TBE (Tris-borate EDTA) buffer (1M Tris, 0.9M Boric acid, 0.01M EDTA) (Invitrogen, CAT-nr.: 15581-044).